



Provided by the author(s) and University of Galway in accordance with publisher policies. Please cite the published version when available.

Title	Calcite sealing in a fractured geothermal reservoir: Insights from combined EBSD and chemistry mapping
Author(s)	McNamara, David D.; Lister, Aaron; Prior, Dave J.
Publication Date	2016-05-10
Publication Information	McNamara, David D., Lister, Aaron, & Prior, Dave J. (2016). Calcite sealing in a fractured geothermal reservoir: Insights from combined EBSD and chemistry mapping. <i>Journal of Volcanology and Geothermal Research</i> , 323, 38-52. doi: http://dx.doi.org/10.1016/j.jvolgeores.2016.04.042
Publisher	Elsevier
Link to publisher's version	https://doi.org/10.1016/j.jvolgeores.2016.04.042
Item record	http://hdl.handle.net/10379/6726
DOI	http://dx.doi.org/10.1016/j.jvolgeores.2016.04.042

Downloaded 2024-05-14T12:38:47Z

Some rights reserved. For more information, please see the item record link above.



1 **Calcite sealing in a fractured geothermal reservoir: Insights from combined EBSD and**
2 **chemistry mapping**

3

4 David D. McNamara, GNS Science, Lower Hutt, New Zealand

5 Aaron Lister, Department of Geology, University of Otago, Dunedin, New Zealand

6 Dave J. Prior, GNS Science, Department of Geology, University of Otago, Dunedin, New

7 Zealand

8

9 Corresponding author: D. D. McNamara, 1 Fairway Drive, GNS Science, Lower Hutt, New

10 Zealand, 5040. (d.mcnamara@gns.cri.nz)

11

12

13

14

15

16

17

18

19

20

21

22

23

24

25 **Abstract**

26

27 Fractures play an important role as fluid flow pathways in geothermal resources hosted in
28 indurated greywacke basement of the Taupo Volcanic Zone, New Zealand, including the
29 Kawerau Geothermal Field. Over time, the permeability of such geothermal reservoirs can be
30 degraded by fracture sealing as minerals deposit out of transported geothermal fluids. Calcite
31 is one such fracture sealing mineral. This study, for the first time, utilises combined data from
32 electron backscatter diffraction and chemical mapping to characterise calcite vein fill
33 morphologies, and gain insight into the mechanisms of calcite fracture sealing in the Kawerau
34 Geothermal Field. Two calcite sealing mechanisms are identified 1) asymmetrical syntaxial
35 growth of calcite, inferred by the presence of single, twinned, calcite crystals spanning the
36 entire fracture width, and 2) 3D, interlocking growth of bladed vein calcite into free space as
37 determined from chemical and crystallographic orientation mapping. This study also
38 identifies other potential uses of combined EBSD and chemical mapping to understand
39 geothermal field evolution including, potentially informing on levels of fluid supersaturation
40 from the study of calcite lattice distortion, and providing information on a reservoir's history
41 of stress, strain, and deformation through investigation of calcite crystal deformation and
42 twinning patterns.

43 **Introduction**

44

45 Development of natural and enhanced geothermal resources, hosted in crystalline, volcanic,
46 plutonic or, metamorphic basement reservoirs, has increased over recent years [Wood et al.,
47 2001; Asanuma et al., 2005; Sausse et al., 2006; Blackwell et al., 2007; Bertani, 2012]. In
48 these reservoir rocks, permeability is dominated by faults and fractures, with small

49 contributions made by primary permeability [Brace, 1980; Davatzes and Hickman, 2010a;
50 Dezayes et al., 2010]. As such, the study of how these structures are generated, their
51 properties (e.g. orientation, spatial distribution, aperture, orientation with respect to the stress
52 field), how they become filled with precipitated minerals, and their crack-seal cycle history is
53 vital to understanding the evolution of geothermal systems and to their successful
54 development. Progressive fracture sealing (i.e. vein formation) is known to create barriers
55 and baffles to fluid flow in a geothermal reservoir, decreasing overall permeability and
56 limiting the reservoir's effectiveness as a resource [Batzle and Simmons, 1976; Dobson et al.,
57 2003; Genter et al., 2010]. Study of this sealing process is vital to discerning the evolution
58 and sustainability of fractured geothermal systems.

59

60 Fracture sealing creates veins which can be used to determine aspects of the geological
61 history of the host rock. The mineralogy, geochemistry, microstructure, and fluid inclusion
62 analysis of vein minerals provides information on pressure and temperature conditions of the
63 reservoir rock, stress and strain that was occurring at or after the time they were precipitated,
64 and on the composition and origin of related fluids. Vein formation (fracture sealing) is
65 achieved by the precipitation of minerals from the circulating fluids, or from water-rock
66 interactions, within geothermal systems, and can occur as a single precipitation event or as
67 multiple crack-sealing events [Ramsay, 1980]. Evidence for multiple sealing events comes
68 from observation of multiple mineral phases, or sequential depositions of the same mineral
69 phase in a vein. The classification of veins can be broken into i) syntaxial, ii) stretching, iii)
70 antitaxial, and iv) pressure shadows/fringes (Figure 1) [Bons et al., 2012]. Syntaxial veins
71 form where mineral growth occurs from one of or both fracture faces toward the centre, with
72 crystals often becoming elongate in the growth direction. Syntaxial vein minerals often show
73 lattice preferred orientations that strengthen with distance from the fracture wall as growth

74 competition eliminates those crystals not oriented to the fast growth direction [Cox and
75 Etheridge, 1983; Bons, 2001; Nüchter and Stöckhert, 2007; Okamoto and Sekine, 2011].
76 Stretching veins grow in a similar way to syntaxial veins [Durney and Ramsay, 1973] but the
77 crack surface cuts through previously precipitated vein crystals (localised stretching veins) or
78 wall rock (delocalised stretching veins) as opposed to the mineral growth surface. Due to
79 their similarity a continuum exists between syntaxial and stretching veins. Localised
80 stretching veins can seal a crack from both crack surfaces (bitaxial) or from one surface
81 (unitaxial) [Hilgers et al., 2000]. Antitaxial veins grow from a median suture in a fracture
82 toward the fracture walls and usually contain fibrous crystals. They are defined by the
83 presence of a median line/zone across which two-fold rotational symmetry is often observed
84 in the fibre pattern. It is thought that antitaxial veins grow by crack-seal mechanisms, or that
85 growth occurs on the closed interface between vein and wall rock. Antitaxial vein growth is
86 also possible as a result of crystal growth, in a diffusional mass transfer (DMT) system,
87 exerting outward force that pushes the wall rock apart [Wiltchko and Morse, 2001]. Pressure
88 shadows/fringes are a unique type of vein that forms in pressure shadows occurring next to a
89 rigid object in a deforming material.

90

91 Determination of mineral sealing processes from microstructural and chemical data is made
92 difficult due to the processes being highly sensitive to a wide range of factors; degree of fluid
93 supersaturation, anisotropic growth kinetics (mineral growth), rates of local deformation, and
94 rates of fluid transport [Hilgers et al., 2004]. Calcite is a common mineral in many geological
95 systems and geothermal reservoirs are no exception. Calcite is usually found in geothermal
96 systems with temperatures of ~140-300°C and where fluids have high concentrations of
97 dissolved CO₂ [Simmons and Christenson, 1994; Browne, 1978] occurring both as a
98 replacement of parent rock mineral phases, or as cement or vein fill. Hydrothermal calcite

99 veins have been reported in geothermal systems in North America [Batzle and Simmons,
100 1976; Dobson et al., 2003], the granite, enhanced geothermal reservoir of Soultz-sous-Forêts
101 [Hébert et al., 2011], and in several geothermal fields located in the Taupo Volcanic Zone
102 (TVZ), New Zealand [Krupp and Seward, 1987; Hedenquist, 1990; Wood et al., 2001]. The
103 precipitation of hydrothermal calcite is controlled dominantly by the movement of CO₂ in the
104 reservoir as governed by boiling, dilution, and condensation, and to a lesser extent by pH,
105 temperature, and the aqueous calcium ion activity [Fournier, 1985; Simmons and
106 Christenson, 1994]. As a result, calcite is a highly reactive mineral in a geothermal system
107 such that varying temperature profiles along fluid flow pathways create zones where it can be
108 dissolved and zones where it can be precipitated. Colder, circulating fluids often result in
109 calcite dissolution, which, due to calcite's retrograde solubility (decreases with increasing
110 temperature), is then precipitated back out elsewhere as the circulating fluid temperature
111 increases [André et al., 2006]. Platy calcite (also known as bladed calcite) is commonly found
112 in veins and voids in geothermal reservoir rocks and is the result of precipitation from boiling
113 fluids through the exsolution of CO₂. Observations of bladed calcite in geothermal wells are
114 made by Tulloch [1982] who noted that the platy crystals grow outward from the walls in a
115 direction perpendicular to the c-axis at a rate of ~0.1mm/day.

116

117 The common occurrence of calcite as a fracture sealing mineral in geothermal fields makes it
118 an ideal case study for examining hydrothermal fracture sealing. This work examines calcite-
119 filled fractures from a sample of greywacke reservoir rock from the Kawerau Geothermal
120 Field using, for the first time, combined chemical mapping techniques (cathodoluminescence
121 (CL) and electron diffraction x-ray (EDX)), and electron backscatter diffraction (EBSD).
122 Similar combinative studies attempting to infer the connection between microstructure and
123 chemistry in veining are rare [Bons et al., 2012 and references therein] and many are more

124 focused on detailed chemical and isotopic analyses [Barker et al., 2006; Barker et al., 2009].
125 This paper aims to utilise these combined techniques to determine how hydrothermal calcite
126 growth occurs in geothermal fractures, explore what the microstructure can tell us about the
127 crack-seal evolution of the greywacke basement of the Kawerau Geothermal Field, and the
128 implications this may have for reservoir permeability.

129

130 *Geological Setting*

131

132 The Kawerau Geothermal Field is the most northern, active, high temperature (>300°C),
133 geothermal field in the TVZ (Figure 2). The TVZ represents the active part of the Central
134 Volcanic Region (CVR), an extensional intra-arc basin formed as a result of subduction of
135 the Pacific Plate beneath the North Island of New Zealand [Wilson et al., 1995; Cole and
136 Spinks, 2009; Begg and Mouslopoulou, 2010; Rowland and Simmons, 2012]. The TVZ is
137 segmented structurally, by offsets in its rift axis [Rowland and Sibson 2001], and
138 magmatically, such that the central TVZ is dominated by rhyolitic volcanism, while the north
139 and south portions experience andesitic-dacitic volcanism [Rowland and Simmons, 2012;
140 Wilson et al, 1995]. Rifting commenced 1-2 Ma and continues to the present day with
141 extension rates decreasing from ~15 mm/yr at the coast of the Bay of Plenty to ~3 mm/yr
142 near the rift termination (south of Lake Taupo) [Villamor and Berryman, 2001; Wallace at
143 al., 2004; Begg and Mouslopoulou, 2010; Chambefort et al., 2014]. Extension in the TVZ is
144 accommodated by the Taupo Rift, a series of dominantly NE-SW striking, normal faults with
145 a vertical maximum principal stress (σ_1/S_v), a NW-SE extension/minimum horizontal stress
146 direction (σ_3/S_{hmin}), and a NE-SW maximum horizontal stress direction (σ_2/S_{Hmax}) [Nicol et
147 al., 2006, Hurst et al., 2008, McLean and McNamara et al., 2011; Wallis et al., 2012;
148 Townend et al., 2012; McNamara et al., 2015].

149

150 The Whakatane Graben, which subsides at rates >0.8 m/ky [Nairn and Beanland, 1989], is
151 situated where the normal faulting of the TVZ intersects with the dominantly strike slip faults
152 of the North Island Dextral Shear Belt [Begg and Mouslopoulou, 2010; Villamor et al.,
153 2011]. The Kawerau geothermal reservoir is located within the Whakatane Graben where
154 rhyolite dominated volcanism of the central TVZ transitions into the andesite-dacite
155 volcanism of the north TVZ segment [Wilson et al., 1995; Nairn, 2002]. The geothermal
156 resource is hosted in Mesozoic greywacke basement composed of medium-grained, andesite-
157 dacite sourced sandstones with minor argillite and chert. The hosting basement terrane for the
158 Kawerau geothermal resource has been debated to be either the Torlesse [Wood et al., 2001]
159 or the Waipapa [Adams et al., 2009]. It is thought that the transition between basement
160 greywacke terranes in the TVZ occurs under or near the Kawerau Geothermal Field [Adams
161 et al., 2009; Leonard et al., 2010; Milicich et al., 2013]. The geothermal reservoir is overlain
162 by ~ 1 km of Quaternary volcano-sedimentary deposits. Fluid flow within the greywacke
163 basement of the Kawerau system is dominated and controlled by a series of faults and
164 fractures as evident from NE-SW trending lineaments of hydrothermal features [Christenson,
165 1987], the spatial relation of structures imaged with borehole viewers to zones of
166 permeability (as measured by pressure, temperature, and fluid velocity logs) [Wallis et al.,
167 2012], and the low permeability of the intact greywacke rock itself [Christenson, 1987;
168 McNamara et al., 2014]. Geothermal well performance indicates that while the north of the
169 Kawerau Geothermal Field hosts permeability controlled by active structures, similar
170 structures present in the south of the field, are likely inactive and sealed by hydrothermal
171 mineral deposition, thus restricting permeability in this area [Christenson, 1997; Bignall and
172 Milicich, 2012; Milicich et al., 2013].

173

174 ***Sample Petrography***

175

176 A sample of un-oriented, greywacke basement drill-core from well KA30 (comprising the
177 interval 1098-1100 mRF), in the southern area of Kawerau Geothermal Field, was utilised for
178 this work. A piece of the drill-core, displaying several intersecting veins, was thin-sectioned
179 (Figure 3). The greywacke is a clast supported, matrix poor, medium to coarse grained
180 greywacke sandstone (0.25 – 1.5 mm) consisting of subangular - subrounded detrital quartz
181 (10%), plagioclase and biotite/phlogopite (30%), and lithic fragments (50%). Lithic
182 fragments include porphyritic lavas, rare plutonic fragments, and siltstone and sandstone
183 fragments. The matrix is composed of indurated clay/silt. This greywacke is moderately
184 altered with a hydrothermal assemblage of chlorite, leucoxene (a granular alteration product
185 of titanium-rich minerals), hydrothermal clays, and minor amounts of wairakite (zeolite;
186 $\text{Ca}_8(\text{Al}_{16}\text{Si}_{32}\text{O}_{96}) \cdot 16\text{H}_2\text{O}$), epidote and disseminated pyrite.

187

188 The greywacke sample used in this study contains a complex set of cross cutting, mineralised
189 fractures filled with calcite, wairakite, and small amounts of pyrite (Figure 3). The youngest
190 fracture set tends to be wider (~1 - 1.5 mm) than the older fractures they cross-cut and
191 contain calcite as their only mineral fill. Calcite in these veins are either elongate (1 - 1.5
192 mm) in appearance (a texture known as bladed calcite), particularly in the wider veins, or
193 have a blocky form. Smaller calcite crystal sizes, with irregular shape are observed nearer the
194 fracture walls. Older fracture generations are filled with mixtures of calcite and wairakite
195 noted to be in textural equilibrium [Christenson, 1987]. Some of these vein textures show
196 wairakite at fracture edges with a central calcite fill (Figure 3). The fracture fill sequences
197 documented here are similar to those described by Absar and Blattner [1985], though we note
198 the lack of prehnite in our study sample.

199

200

201 Fracturing in the Kawerau Geothermal Field reservoir is thought to be hydraulic in origin.
202 This is supported by observed vein mineral assemblages which follow models for
203 mineralisation in hydraulic-fracturing [Phillips, 1972; Hedenquist and Henley, 1985] in rock
204 with high tensile strength and low intrinsic permeability, both of which are true of the
205 greywacke basement at Kawerau [McNamara et al., 2014]. Additionally, veins are often
206 noted to contain wall-rock fragments, providing evidence of the explosive nature of the
207 fracturing events [Christenson, 1987]. The greywacke wall rock proximal to all fractures in
208 the studied sample shows damage (shattered quartz, feldspar, and lithic grains, and narrow,
209 micro-fractured, damage zones around the main fracture structures) and supports
210 interpretation of these fractures forming during an explosive, hydrofracturing process
211 [Christenson, 1987]. This effect is more pronounced around the older, wairakite/calcite filled
212 fractures, than around the younger, bladed calcite filled fractures. The younger fracture
213 generation examined in this study cross-cuts older fractures at a high angle and also cuts
214 across larger quartz and lithic grains of the greywacke rock. Where shear markers can be
215 identified either side of these younger fractures, small lateral offsets can be observed. The
216 most obvious lateral offset noted is where a younger generation fracture offsets an older
217 wairakite/calcite filled fracture by ~ 0.25 mm (Figure 3c), indicating a shear component to
218 the younger fracture.

219

220 Fluid inclusion homogenisation temperatures, freezing point depression data, and the
221 presence of liquid and vapour rich fluid inclusions, indicate that Kawerau basement vein
222 calcite deposited from boiling fluids [Christenson, 1987]. The implication of a boiling parent

223 fluid is that the confining pressure in the fracture was likely less than the hydrostatic pressure
224 at depth. However the modal homogenisation temperatures noted by Christenson [1987] lie
225 above the boiling point curve for water, indicating that fracture channels were also, at times,
226 overpressured (above local hydrostatic). It is thought that this over pressurisation is a
227 prerequisite for initiating the hydraulic fracturing in the Kawerau Geothermal Field in the
228 first place. A combination of overpressured fluid in the fractures, and volcanic processes
229 associated with Putauaki are thought to be responsible for the hydro-fracturing [Hedenquist
230 and Henley, 1985; Phillips, 1972; Christenson, 1987]. Hydrofracturing, which resulted in a
231 sudden pressure drop, is responsible for the instantaneous flashing, and rapid supersaturation
232 of calcite in the boiling fracture fluid, which resulted in rapid precipitation of calcite on the
233 fracture walls, often with bladed crystal morphology [Christenson, 1987]. Bladed calcite in
234 veins at Kawerau Geothermal Field are thought to have undergone rapid growth due to
235 observed pitted surfaces under SEM [Christenson, 1987], and observations of rapid growth of
236 bladed calcite (~0.1 mm/day) in flowing wells at Kawerau [Tulloch, 1982].

237

238 Temperature conditions of calcite formation in veins at Kawerau Geothermal Field have been
239 determined from fluid inclusion and stable isotope studies [Christenson, 1987; Absar, 1988].
240 Temperatures for the deposition of the calcite from fluid inclusion measurements have not
241 been made on the vein samples investigated in this paper but have been reported from bladed
242 calcite veins in nearby wells at similar depths [Christenson, 1987]. Fluid temperatures during
243 bladed calcite precipitation are tentatively placed at ~270-305 °C. Isotope data (δO^{18}) from
244 this calcite precipitation event indicates precipitation from meteoric fluids with a magmatic
245 component [Absar, 1988]. The formation depth of the youngest vein generation (bladed
246 calcite) in the investigated sample can be assumed to be ~1100 m, assuming that the bladed
247 calcite precipitation event likely represents, at its oldest, the initiation of the modern

248 geothermal system in Kawerau (~16000 yrs), and little erosion of cover material has occurred
249 [Milicich et al., 2013]. This postdates the deposition of nearly all the volcanosedimentary
250 units that overlie the greywacke basement in this area [Milicich, 2014]. Assuming a vein
251 formation depth of 1100 m, fluid temperatures of ~270-305 °C, water density values of 1531-
252 1846 kg/m³, and the fact that bladed calcite precipitated from fluid under confining pressures
253 lower than the hydrostatic pressure, an estimation of vein formation pressure is ~16-20 MPa.
254 Attempting to determine the vein formation conditions for the older wairakite-calcite vein is
255 more difficult. Wairakite, commonly found in hydrofractures in geothermal fields, is known
256 to form when measured temperatures are in excess of 160°C at Kawerau, and the later calcite
257 in this vein, likely precipitated at temperatures similar to those of the younger vein
258 (>~270°C) [Christenson, 1987]. Isotopic studies (δO^{18}) of wairakite-prehnite veins [Absar,
259 1988] suggest higher fluid temperatures of 280-300 °C and that this vein fill represents an
260 earlier deposition event from meteoric fluids that predates the deposition of calcite. The
261 timing of this older veining event remains equivocal and the depth of its formation, and thus
262 pressure conditions, are undetermined.

263

264 **Methodology**

265

266 ***Sample Preparation***

267

268 A 30µm thick thin section (Figure 3b) was mechanically and chemically polished using
269 diamond pastes down to 1µm followed by colloidal silica. This process minimised negative
270 effects of surface damage and topography on EBSD mineral indexing [Prior et al., 1996]. The

271 edges of the prepared specimen were painted with carbon and the sample surface was carbon
272 coated (~10nm thick) to prevent charging in the SEM.

273

274 ***Electron Backscatter Diffraction (EBSD)***

275

276 EBSD is a technique capable of rapid acquisition of large crystallographic orientation
277 datasets of a rock's mineral phases [Prior et al., 1999]. EBSD carried out in this work was
278 performed using a Zeiss Sigma variable pressure field emission gun SEM fitted with an
279 Oxford Instruments Nordlys F EBSD camera and an XMax 20 silicon drift EDX detector,
280 located at the Otago Centre for Electron Microscopy (OCEM) at the University of Otago,
281 Dunedin. To collect EBSD patterns, the thin section was tilted 70° to the incoming electron
282 beam allowing for a diffraction pattern to be generated on a phosphor screen. EBSD was
283 carried out using an acceleration voltage of 30 kV, beam current of ~90nA, and a working
284 distance of ~20 mm. Both EBSD and EDX data were collected using Oxford instruments
285 AZTec software which undertook initial processing for both techniques. The mapped EBSD
286 data was processed with HKL Channel5 software using methods comparable to Bestmann
287 and Prior [2003].

288

289 ***Energy Dispersive X-Ray Spectroscopy (EDX) and Cathodoluminescence (CL)***

290

291 EDX data were collected using Oxford Instruments AZTEC software with a XMAX20
292 silicon drift detector. Full spectrum EDX data were collected on a grid using an accelerating
293 voltage of 15 to 20 kV and ~ 1-10 nA of beam current. Spectra (including map data) were

294 processed using the TruMap and QCAL procedures within the AZTEC software. Map data
295 presented here show counts within $K\alpha$ energy windows corrected for peak overlaps and
296 background counts.

297

298 CL images were taken using a Technosyn cold cathode stage mounted on an Olympus BX41
299 microscope with a trinoc head fitted with a digital camera. The CL apparatus was operated
300 under vacuum (0.05-0.08 Torr / 17-20 V) at an accelerating voltage of 15-20 kV and a beam
301 current of 550-600 μA .

302 **Results**

303

304 *Cathodoluminescence (CL)*

305

306 Figure 4 shows CL images of the fractures in the sample: colours vary from fracture to
307 fracture. The youngest generation of fracturing shows bright, yellow/orange coloured calcite
308 (Figure 4b) while the older fractures, cross-cut by the younger fractures, contain wairakite
309 (dull, purple/blue CL colours) and calcite (dull, darker orange/red CL colours) (Figure 4c).
310 Individual calcite crystals in all fracture generations show variation of the orange/red CL
311 colours, implying they are chemically zoned. Yellow cathodoluminescence in calcite is linked
312 to higher Mn content, whereas red CL response is proportional to Fe content [Long and
313 Agrell, 1965]. *Visa versa*, the more red the CL colour the higher the Fe content and lower the
314 Mn content.

315

316 Zonation in CL is more pronounced in calcite crystals sealing the younger generation of
317 fractures (Figure 4e). These calcite crystals show complicated zonation patterns. In some
318 elongate calcite crystals, concentric zonation stretches along the crystal long axes in bands
319 (Figure 4e, 11). This concentric banding varies in width along the crystal axes; thinner along
320 the long edges of the crystal and thicker at either end of the elongated crystals (Figure 11). In
321 some places along the crystal long axes a particular zonation band grows outward
322 perpendicular to the long axes, creating a 'bulging' morphology (Figure 4e). In elongate
323 crystals that have such bulges, zonation appears as successive bands progressing outward
324 from the core of the crystal and into the bulging area (Figure 4e). Older fracture calcite
325 crystals are zoned but have no discernible zonation pattern (Figure 4d).

326

327 *Energy Dispersive X-Ray Spectroscopy (EDX)*

328

329 EDX elemental count maps were generated for Area '1' (Figure 4b, Figure 5a), the
330 generation of younger veins filled with bladed calcite (measurement point every 2 μ m), and
331 Area '2' (Figure 4c, Figure 5b), the older fracture generation containing wairakite and calcite
332 (measurement point every 2 μ m). EDX maps of Area 1 (Figure 5a) show the same chemical
333 zonation patterns observed in CL (Figure 4b). EDX maps of Area 2 do not show the zonation
334 patterns observed from CL (Figure 4c). Ca and Al EDX count maps of Area 2 delineate the
335 older wairakite vein fill from the younger calcite fill due to the differences in their chemical
336 compositions (Figure 5b).

337

338 An EDX linescan (in weight%) of a profile across zoned calcite crystals in the younger vein
339 generation is shown in Figure 6 next to corresponding CL and BSE images of the zonation.
340 This plot shows that darker grey colours on the BSE image corresponds to purer calcite
341 (CaCO_3), whereas lighter grey colours contain higher levels of Fe+Mn. Correlation of the
342 linescan to the CL image shows more intricate chemical variation. Zones associated with
343 purer CaCO_3 (seen on BSE image) appear as variable shades of dark red or orange CL
344 colours. This implies additional chemical variation in these calcite crystals beyond Mn+Fe.
345 Other major elements (O, C, Mg, Si, Al, Na) are ruled out as they display no variation after
346 investigation by EDX. In places the Fe/Ca ratio is higher than the Mn/Ca ratio which is
347 related to darker red CL coloured zones (~138-180 μm , 1029-1050 μm ; Figure 6).

348

349 *Electron Backscatter Diffraction (EBSD)*

350

351 EBSD maps of calcite crystals from both the youngest and an older generation of sealed
352 fractures are shown in Figure 7 and 9, respectively. EBSD grain maps of the younger fracture
353 sealed by calcite mineralisation (Figure 7) show predominantly large, elongate crystals of
354 calcite (~0.5-2 mm long), and less frequent, large, blocky calcite forms (~0.5 mm long).
355 Smaller-sized calcite crystals (~0.05-0.25 mm) are predominantly found near the fracture
356 walls. Elongate calcite crystals are green and blue in the IPFZ map (Figure 7b); the c-axes are
357 at low angles to the thin section plane and perpendicular to crystal long axes (i.e. basal plane
358 trace lies parallel to long axis). Calcite crystals with a blocky form have pink, orange, and red
359 colours in the IPFZ map (Figure 7b) corresponding to c-axes at high angles to the thin section
360 plane. Most elongate calcite crystals show continuous distortion (low angle ($<2^\circ$)
361 misorientation) along their long axes while blocky calcite crystals show no measureable

362 internal crystal distortion (Figure 7c). Some calcite crystals (Figure 7a, 7c) have 2°-5° sub-
363 grain boundaries (displaying rotation around the m axes), and 5°-10° sub-grain boundaries
364 (displaying rotation around the <02-21> axis) (Figure 7d). A small number of misorientation
365 angle boundaries of 75°-80° are observed, with rotation axes indicative of calcite e-twins
366 ($20\bar{2}1$, Figure 7d). One point per grain calcite pole figures show calcite has a weak LPO in
367 this fracture with the c-axes preferentially oriented perpendicular to the fracture wall.
368 Misorientation angle distribution analyses (Figure 10a, 10b) shows little difference between
369 random and neighbour pair misorientation angle distributions apart from a slightly higher
370 frequency of low angle (<10°) and 75°-80° angle neighbour misorientations than the random
371 frequency.

372

373 EBSD mapping of the older calcite vein (Figure 9) shows calcite crystals of a single
374 orientation have grown across the fracture. Calcite crystals commonly contain either one
375 (smaller crystals ~0.13 mm) or two twin (larger crystals, ~0.63-0.75 mm) sets and one large
376 grain (~0.88 mm) contains three sets of twins. All twin sets in these calcite crystals are e-
377 twins. The host calcite crystals display continuous distortion (<2°). Other host calcite
378 microstructures, such as common 2°-5° and rare 5°-10° sub-grain boundaries, are present and
379 have dominant <a> rotation axes (<11-20>). Misorientation angle distribution analyses
380 (Figure 10c, 10d) shows a slightly higher frequency of low angle (<10°) neighbour
381 misorientations than the random distribution, similar to the younger calcite vein.

382

383 **Discussion**

384

385 *Insights into Calcite Growth in a Geothermal Fracture*

386

387 The bladed calcite crystals in the younger vein investigated here do not appear to have grown
388 following the typical symmetrical, vein-normal, growth directions expected in crack-seal
389 fractures [Bons et al., 2012; Figure 1]. Rather the crystal morphology of this fracture implies
390 calcite nucleated and grew outward in a number of directions with preferred crystallographic
391 orientation, filling in available space, and eventually sealing the fracture with a 3D
392 interlocking set of elongated crystals. The chemical zonation patterns observed in bladed
393 calcite crystals, due to the variable inclusion of Fe and Mn into the calcite crystal structure as
394 it precipitated, infer that they grew in a free fluid with changing composition [ten Have and
395 Heijnen], and that they grew preferentially outward in two opposite directions (usually
396 parallel to the fracture length) producing bladed morphologies. These observations, combined
397 with information from EBSD texture component maps (Figure 11), and the presence of a
398 weak calcite vein LPO, show that these elongate calcite crystals grew outward from a central
399 core along the crystallographic m axis, such that the c-axes are perpendicular to the fracture
400 wall. This is similar to another observation made of bladed calcite crystal growth in a
401 geothermal well pipe, where crystals grew perpendicular to their c-axis [Tulloch, 1982], and
402 to records of elongate calcite vein growth in other studies [Bradshaw and Phillips, 1964;
403 González-Casado and Garcia-Cuevas, 1999; Friedman and Higgs, 2013].

404

405 Further evidence of a three-dimensional interlocking morphology for these calcite crystals are
406 the ‘cross-cutting’ relationship that can be observed from EBSD maps (Figure 7, 11). This
407 and other aspects of the crystal texture in this vein, such as the chemical zonation patterns,
408 suggest that calcite precipitated and grew long in their preferred direction (parallel to the

409 plane of the vein) and began to experience space competition in those directions. In effect,
410 calcite growth along the fast axes became locked as growing crystals intercepted each other.
411 This left calcite with the option of growing outward parallel to their c-axes giving the bladed
412 crystals their often observed 'bulge' morphology (Figure 11). This continued, along with new
413 calcite crystal nucleation (evidenced by small calcite crystals within the fracture), until nearly
414 all the available fracture space was filled.

415

416 Potential models for the calcite morphology and microstructure observed in the younger vein
417 investigated here include: growth of calcite crystals in 3D from numerous sites at the fracture
418 wall, and calcite replacement of a pre-existing carbonate vein fill. The latter is unlikely given
419 that bladed calcite is indicative of the near-instant, flash-sealing of hydro-fractures after they
420 formed [Christenson, 1987]. Progressive 3D growth from a number of sites provides a more
421 probable method to generate the observed vein texture here. The walls of the investigated
422 vein are irregular in shape as observed from hand-specimen and thin section (Figure 3). This
423 would have provided a number of variably oriented surfaces that allowed calcite crystals to
424 nucleate, with some then growing rapidly along their m-axes outward and into the open
425 fracture space, with their long-axes preferably aligned to a given surrounding stress field,
426 while others form smaller calcite crystal clusters at the fracture wall as observed (Figure 7).
427 Fast growing elongate calcite crystals would experience space competition with each other,
428 growing elongate around each other, providing the interlinked bladed texture observed.

429

430 Calcite morphologies in the older vein investigated do not have the bladed morphologies
431 observed in the younger vein. They appear to have grown across the open width of the
432 fracture as one single crystal, implying that crystal nucleation of calcite in this fracture was

433 syntaxial, with initial growth on the wairakite crystals on one side of the vein wall, followed
434 by asymmetrical growth (i.e. from one wall of the fracture only). Chemical zonation in these
435 crystals does not appear to have a discernible pattern that can be related to growth. We argue
436 here that the calcite in this vein does not represent wairakite replacement as the thin section
437 and SEM observations clearly show textures expected from space infilling, and previous
438 observations that the minerals in these veins are in textural equilibrium [Christenson, 1987,
439 Absar and Blatiner, 1985]. However, further work to determine any potential control
440 wairakite may have on the nucleation, crystal lattice orientation, and growth development of
441 calcite, would benefit from further EBSD study. Initial attempts to do so in this investigation
442 were hindered due to poor EBSD indexing of the wairakite phase.

443

444 Different calcite sealing mechanisms are present in the two different veins. Discerning the
445 dominant cause for this variation is difficult given the large number of variables associated
446 with calcite formation in the Kawerau Geothermal Field and the limitations of currently
447 acquired data. Possible insight may come from cathodoluminescence observations. Rate of
448 calcite crystallisation largely controls the morphology of precipitating calcite crystals [Folk,
449 1974]. Fe and Mn incorporation into calcite can be affected by fluid composition [Wogelius
450 et al., 1997], and also by calcite precipitation rates and temperature. Both the Fe and Mn
451 content in calcite increases with decreasing precipitation rate, or increasing temperature, with
452 the ratio of Mn/Fe increasing with decreasing precipitation rates [Dromgoole and Walter,
453 1990]. The observed variation in cathodoluminescence between calcite in the older and
454 younger vein may have resulted from different precipitation rates, which influenced the style
455 of calcite growth and thus fracture sealing. We rule out the control of temperature on
456 cathodoluminescence here as the younger and older vein calcite is thought to have precipitated
457 from fluids of similar temperatures [Christenson, 1987]. We note here that relationships

458 between Fe and Mn incorporation into calcite and precipitation rates have not been tested at
459 the geothermal fluid temperatures the calcite in this study precipitated from, and further
460 research into that relationship is required.

461

462 Continuous lattice distortion across calcite crystals is observed in both fractures. This may
463 indicate low levels of dislocation creep activity, enough to subtly deform the crystal lattice
464 but not enough to create and migrate subgrain boundaries. However, simple grain growth can
465 also generate the continuous lattice distortion observed here. Studies of the kinetics and
466 mechanisms of carbonate/calcite growth show that for low levels of supersaturation in the
467 precipitating fluid, {10-14} calcite face growth occurs at surface defects on the deposition
468 surface, including screw dislocations, i.e. defect-originated growth, and at higher
469 supersaturations growth progresses via a homogeneous surface nucleation process
470 (Lefauchaux et al., 1973; Lefauchaux and Robert, 1977; Teng et al., 2000; Xu et al., 2014). A
471 crystal growth explanation for the observed diffuse misorientation profiles in calcite crystals
472 in the younger fracture is supported by its spatial correlation with calcite crystal growth
473 directions (Figure 11). Continuous distortion is only observed in elongate calcite crystals,
474 with crystal misorientation increasing away from the crystal core (as determined from calcite
475 CL maps). Thus as the calcite crystal grows, becoming elongate along its preferred growth
476 axis (the m axis), it accumulates small lattice defects that subtly alter the crystal lattice
477 orientation. This observation infers that the bladed calcite in this vein precipitated from
478 boiling fluids with low levels of supersaturation with respect to calcite. This model of
479 variable crystal growth direction bears similarities to textures noted in other vein crystal
480 growth [Urai et al., 1991; Bons, 2001], and to mineral scale build up inside autoclaves
481 [Timms et al., 2009].

482 ***Geothermal Reservoir Conditions from Vein Calcite Deformation***

483

484 Calcite crystals in both fractures contain low angle (2° - $<10^\circ$ misorientation) sub-grain
485 boundaries. While these sub-grain boundaries are restricted to a few calcite crystals in the
486 younger fracture, they are common in the calcite crystals of the older fracture. Subgrain
487 development may be the result of deformation via dislocation creep in these calcite crystals,
488 or, as discussed earlier, potentially a result of calcite growth incorporating surface defects. If
489 we assume dislocation creep as the cause of subgrains in calcite we can conclude that crystals
490 in the older fracture have undergone greater deformation than crystals in the younger fracture.
491 Further to this, the misorientation axes of the subgrain boundaries found in the older and
492 younger calcite crystals are different. The youngest fracture calcite has dominant *m* (for
493 subgrain boundaries of 2 - 5° misorientation) and *sd* $\langle 02\text{-}21 \rangle$ (for subgrain boundaries of 5 -
494 $<10^\circ$ misorientation) rotation axes. Rotation axes are dominantly *a* in calcite in the older
495 fracture for all subgrain boundary categories. As such we can propose that that not only has
496 calcite in each fracture generation undergone different amounts of dislocation creep, the slip
497 systems by which it was operating also vary. The operation of various slip systems in calcite
498 has been shown to be temperature dependent under particular strain rates and so documenting
499 which ones are in operation in geothermal veins can potentially inform us of deformation and
500 thermal history of a rock (De Bresser and Spiers, 1997). Application of this theory to calcite
501 veins in geothermal reservoirs bear further study as it may prove a useful tool for estimating
502 the thermal evolution of the resource.

503

504 Measuring the orientation of calcite c-axes allows determination of the 'tension' direction the
505 rock was under [González-Casado and García-Cuevas, 1999]. The calcite sealing the

506 youngest fracture generation shows a weak LPO, with calcite c-axes aligned perpendicular to
507 the fracture wall (Figure 13). As the sample investigated here does not have a geographical
508 reference frame, we cannot infer the geographical extension direction associated with the
509 formation of this fracture. We can, however, state that the extension direction during the time
510 of calcite crystal growth in this fracture was perpendicular to the fracture length. An
511 extension direction perpendicular to the fracture walls, in combination with the observed
512 small, lateral offset of an older structure indicates this fracture was created through a
513 combination of extension (mode I) and shear (mode II/III) kinematics.

514

515 Calcite crystals in both the older and younger fractures contain e-twins. Twinning density is
516 higher in calcite crystals in the older fracture than the younger fracture. Mechanical twinning
517 is a common microstructure in calcite and often operates as a deformation mechanism
518 [Barber and Wenk, 1979; Burkhard, 1993; Larsson and Christy, 2008]. The relationship
519 between calcite twin structures, temperature, and stress and strain makes them useful for
520 determining the magnitudes and orientations of the principal stress axes in tectonic
521 environments [Jamison and Spang, 1976; Laurent et al., 1981; Groshong Jr. et al., 1984;
522 Rowe and Rutter, 1990; Lacombe and Laurent, 1992; Ferrill et al., 2004; González-Casado et
523 al., 2006; Chen et al., 2011]. Certain twinning properties in calcite lend themselves to the
524 determination of stress, for example, determination of strain associated with twinning can be
525 done by measuring the average thickness of twins (the amount of simple shear deformation is
526 proportional to the twin thickness) [Groshong, 1972; Groshong et al., 1984; Ferrill, 1991;
527 Ferrill et al., 2004]. Additionally, paleo-differential stress magnitudes can be determined
528 from log twin density or the percentage of calcite crystals with one, two, or three twin sets
529 [Rowe and Rutter, 1990].

530

531 The lack of twinning in the calcite crystals of the younger vein implies that the rock has
532 experienced little strain since this sealing event. Thus, we suggest that the fracturing
533 represented by the bladed calcite veins, at least for the basement rock in the vicinity of well
534 KA30, marks the last significant brittle deformation event (hydrofracturing associated with
535 volcanic activity of nearby Putauaki). However, the low number of grains captured in this
536 dataset, and the lack of orthogonal sections to investigate, prevents a full strain and stress
537 analysis using calcite twins. A preliminary calculation of the log twin density of calcite
538 crystals in the older vein is presented here in order to highlight the potential of a further, more
539 robust study of this kind in the future. These measurements of calcite twin density do not
540 follow the prescribed methodology in Rowe and Rutter [1990], in that twin densities are not
541 measured from this sample on orthogonal surfaces, rather they have been calculated based on
542 one observed section. Using EBSD maps of the older calcite vein, we measured the number
543 of twins/mm for each calcite crystal, defined by Rowe and Rutter [1990] as the rate of change
544 of the number of lamellae of a given twin set with respect to grain diameter measured normal
545 to the trace of the twin lamellae. This was done for the two twin sets observed, set 1 and set
546 2, with set 1 representing the oldest twinning in these crystals determined from cross-cutting
547 relationships. Differential stress magnitudes are determined from these preliminary calcite
548 log twin density data using the Rowe and Rutter [1990] equation determined from
549 experimental and natural data [1990], assuming that the relationship derived from their study
550 is applicable to all naturally deformed rocks, and that the density of nuclei for twin formation
551 is constant around calcite crystal boundaries.

552

553 Based on the log twin densities from twin set 1, calcite crystals in the older vein have
554 experienced high differential stresses at some stage after the calcite precipitated (~200 - 250
555 MPa \pm 43 MPa) (Figure 12). This differential stress magnitude recorded by calcite in the
556 older vein represents a) the stress required to cause the greywacke rock to hydrofracture
557 resulting in the formation of the younger bladed calcite vein, which may represent the last
558 stage of brittle deformation of the basement rock in this area as discussed previously or b)
559 possible deformation events that occurred after the calcite of the older vein has precipitated
560 but before the hydrofracturing event that generated the younger calcite veins. Assuming that
561 the calcite twinning in the older vein is recording the stress required to generate the younger
562 hydrofracturing, differential stresses high enough to overcome the yield strength of the
563 greywacke (which has UCS values ranging from 164 – 310 MPa) would be required
564 [Richards and Read, 2007; McNamara et al., 2014]). If the twinning in the older fracture
565 calcite is a result of this event then the recorded differential stresses of ~205 MPa seem
566 realistic but a more robust study of the calcite twinning should be carried out before drawing
567 any final conclusions.

568

569 ***Fluid Flow***

570

571 Petrographic, microstructural and chemical mapping of vein fills in geothermal fractures can
572 provide useful information on the evolution of structural permeability in the basement hosted
573 reservoir at the Kawerau Geothermal Field. It is a general concept that progressive
574 mineralisation within a fracture decreases the porosity and permeability of that structure, but
575 only if it ceases to propagate and open, and assuming that fracture opening is not concurrent
576 with mineral precipitation, in which case the structure would potentially host little

577 permeability at all. Given that the generation of the fractures studied here is associated with
578 disruptive, energetic hydrofracturing, it is likely they were initially open to fluid flow. Fluid
579 flow capability of the fractures was then progressively reduced by mineral precipitation, and
580 gradual mechanical closing of these fractures due to post hydraulic fracturing decreased fluid
581 pressure.

582

583 It is thought that as fracture sealing minerals grow from fracture walls there is a tendency for
584 smaller fractures to be sealed off more efficiently and quickly than larger scale fractures. This
585 would lead to wider fractures dominating the structural permeability of a rock (Marrett and
586 Laubach, 1997). Fast rates of bladed calcite growth (~0.1 mm/day) [Tulloch, 1982], would
587 suggest that even wide fractures are sealed quickly. As such, wide fractures may not represent
588 the dominant permeable structures in a geothermal system as has been suggested by other
589 studies [Sheridan et al., 2003; Davatzes and Hickman, 2009; McLean and McNamara, 2011;
590 Wallis et al., 2012]. Observations of the occurrence of wide aperture fractures existing
591 outside permeable zones in geothermal wells have been noted in other studies, supporting this
592 theory [McNamara et al., 2015; Massiot et al., 2015].

593

594 Finally, growth of bladed calcite, despite occurring at rapid rates, has the potential to act as a
595 mechanism by which to preserve or prolong the permeable lifetime of the hydraulic fractures
596 observed at Kawerau. Our microstructural and chemical investigation of bladed calcite
597 crystals shows they can grow quickly from fracture walls to create a complex 3D interlocking
598 structure. Rapid growth of this calcite crystal morphology may serve to prop open these wide
599 fractures, acting against their tendency to close. By propping open the hydraulic fractures,

600 longer time periods of fluid flow are supported until eventually calcite precipitation fills up
601 all available space.

602

603 **Conclusions**

604

605 Observations of calcite crystal morphology, chemical zonation, and crystallographic patterns
606 from two sealed geothermal fractures show different fracture sealing mechanisms in
607 operation; asymmetrical syntaxial growth, and growth in free 3D space. Examination of a
608 larger set of calcite fractures will be required to determine if a preferred calcite sealing
609 mechanism exists in geothermal veins, and whether the sealing mechanisms is dependent on
610 the how the calcite precipitates (e.g. whether boiling conditions are present at the time of
611 calcite growth).

612 Combined EBSD/EDX/CL study of calcite sealed fractures in geothermal reservoirs shows
613 promise as a useful tool in understanding its evolution:

- 614 • Lattice distortion associated with the continual growth of bladed calcite crystals may
615 indicate defect-originated growth. This provides insight into the geothermal fluid
616 conditions that precipitated these crystals as this type of calcite growth occurs from
617 lower levels of supersaturation.
- 618 • The lack of significant twinning and micro-deformation (sign of deformation) in the
619 bladed calcite of the youngest fracture generation implies that this fracture represents
620 the most recent tectonic event strong enough to create new fractures in the basement.
621 The low occurrence of twinning also implies that since this fracture was sealed there

622 has been little strain accumulation in the rock, or if there has none of it is
623 accommodated by the calcite in this fracture.

- 624 • Observations of calcite twinning in older calcite filled fractures may potentially
625 record differential stress magnitudes that this reservoir rock has been subjected to
626 over time. A more in-depth study with appropriate orthogonal sections of these calcite
627 filled fractures is required to obtain more accurate data.
- 628 • Determination of calcite lattice preferred orientations from sealed fractures can
629 provide insight into the tension direction of the structure and possible variation in the
630 orientation of tension over time.

631

632 **Acknowledgements**

633

634 Acknowledgements go to the Geothermal Resources of New Zealand research program at
635 GNS Science and the University of Otago for funding for this work, Ngati Tuwharetoa
636 Geothermal Assets (NGTA) for supplying core samples from Kawerau Geothermal Field and
637 for permission to release this data.

638

639

640

641

642

643

644

645

646 **References**

647

648 Absar, A., P. Blattner (1985), Successive hydrothermal events, as indicated by oxygen
649 isotope composition and petrography of greywacke basement rocks, Kawerau
650 Geothermal Field, New Zealand, *Proceedings 7th New Zealand Geothermal*
651 *Workshop*.

652 Absar, A. (1988), Oxygen isotope and hydrothermal alteration studies at Kawerau and
653 Ohaaki-Broadlands geothermal fields, New Zealand, Ph.D. Thesis, University of
654 Auckland, New Zealand.

655 Adams, C.J., N. Mortimer, H. J. Campbell and W. L. Griffin (2009), Age and isotropic
656 characterisation of metasedimentary rocks from the Torlesse Supergroup and
657 Waipapa Group in the central North Island, New Zealand, *New Zealand Journal of*
658 *Geology and Geophysics*, 52, 149-170.

659 André, L., V. Rabemanana, F. –D. Vuataz (2006), Influence of water-rock interactions on
660 fracture permeability of the deep reservoir at Soultz-sous-Forêts, France,
661 *Geothermics*, 35, 507-531.

662 Asanuma, H., N. Soma, H. Kaieda, Y. Kumano, T. Izumi, K. Tezuka, H. Niitsuma and D.
663 Wyborn (2005), Microseismic monitoring of hydraulic stimulation at the Australian
664 HDR Project in Cooper Basin, *Proceedings World Geothermal Congress 2005*.

665 Barker, S. L. L., S. F. Cox, S. M. Eggins and M. K. Gagan (2006), Microchemical evidence
666 for episodic growth of antitaxial veins during fracture-controlled fluid flow, *Earth and*
667 *Planetary Science Letters*, 250, 331-344, DOI: 10.1016/j.epsl.2006.07.051.

668 Barker, S. L. L., V. C. Bennett, S. F. Cox, M. D. Norman and M. K. Gagan (2009), Sm-Nd,
669 Sr, C and O isotope systematics in hydrothermal calcite-fluorite veins: Implications
670 for fluid-rock reaction and geochronology, *Chemical Geology*, 268, 58-66,
671 doi:10.1016/j.chemgeo.2009.07.009.

672 Batzle, M.L., G. Simmons (1976), Microfractures in rocks from two geothermal areas, *Earth
673 and Planetary Science Letters*, 30, 71-93.

674 Begg, J. G. and V. Mouslopoulou (2010), Analysis of late Holocene faulting within an active
675 rift using lidar, Taupo Rift, New Zealand, *Journal of Volcanology and Geothermal
676 Research*, 190, 152-167, doi:10.1016/j.jvolgeores.2009.06.001.

677 Bertani, R. (2012), Geothermal power generation in the world 2005–2010 update report,
678 *Geothermics*, 41, 1–29, doi:10.1016/j.geothermics.2011.10.001 .

679 Bestmann, M., Prior, D.J. (2003) Intragranular dynamic recrystallization in naturally
680 deformed calcite marble: diffusion accommodated grain boundary sliding as a result
681 of subgrain rotation recrystallization, *Journal of Structural Geology*, 25, 1597-1613.

682 Bibby, H.M., T. Caldwell, F. Davey and T. Webb (1995), Geophysical evidence on the
683 structure of the Taupo Volcanic Zone and its hydrothermal circulation, *Journal of
684 Volcanology and Geothermal Research*, 68, 29–58, doi:10.1016/0377-
685 0273(95)00007-H.

686 Bignall, G. and S. D. Milicich (2012), Kawerau Geothermal Field: geological framework.
687 *GNS Science Consultancy Report 2012/118*, Institute of Geological & Nuclear
688 Sciences, Lower Hutt, New Zealand.

689 Blackwell, D. D., P. T. Negraru and M. C. Richards (2007), Assessment of the enhanced
690 geothermal system resource base of the United States, *Natural Resources Research*,
691 15, 283–308, doi:10.1007/s11053-007-9028-7.

692 Bons, P. D., (2001), Development of crystal morphology during unitaxial growth in a
693 progressively widening vein: I. The numerical model, *Journal of Structural Geology*,
694 23, 865-872, doi:10.1016/S0191-8141(00)00159-0.

695 Bons, P. D., M. A. Elburg and E. Gomez-Rivas (2012), A review of the formation of tectonic
696 veins and their microstructure, *Journal of Structural Geology*, 43, 33-62.

697 Brace, W. F. (1980), Permeability of crystalline and argillaceous rocks, *International Journal*
698 *of Rock Mechanics and Mining Sciences & Geomechanics Abstracts*, 17, 241–251,
699 doi:10.1016/0148-9062(80)90807-4.

700 Bradshaw, R. and F. C. Phillips (1964), X-ray studies of natural fabrics. I. Growth-fabrics in
701 hematite kidney ore and in fibrous calcite, *Mineralogical Magazine*, 36, 70-77.

702 Browne, P.R.L. (1978) Hydrothermal alteration in active geothermal fields, *Annual Review of*
703 *Earth and Planetary Sciences*, 6, 229-250,
704 doi:10.1146/annurev.ea.06.050178.001305.

705 Burkhard, M. (1993) Calcite twins, their geometry, appearance and significance as stress-
706 strain markers and indicators of tectonic regime: a review, *Journal of Structural*
707 *Geology*, 15, 351-368.

708 Chambeft, I., Lewis, B., Wilson, C.J.N., Rae, A.J., Coutts, C., Bignall, G., Ireland, T.R.
709 (2014), Stratigraphy and structure of the Ngatamariki geothermal system from new
710 zircon U-Pb geochronology: Implications for Taupo Volcanic Zone evolution,
711 *Journal of Volcanology and Geothermal Research*, 274, 51-70, doi:
712 10.1016/j.jvolgeores.2014.01.015.

713 Chen, K., Kunz, M., Tamura, N., Wenk, H.-R. (2011) Deformation twinning and residual
714 stress in calcite studied with synchrotron polychromatic X-ray microdiffraction,
715 *Physics and Chemistry of Minerals*, 38, 491-500.

716 Christenson, B. W. (1987), Fluid - mineral equilibria in the Kawerau hydrothermal system,
717 Taupo Volcanic Zone, New Zealand, Ph.D. Thesis, University of Auckland, New
718 Zealand.

719 Christenson, B. W. (1997), Kawerau Geothermal Field: Geochemical structure of the
720 reservoir and its response to exploitation, *Transactions of the Geothermal Resources*
721 *Council*, 21, 17-24.

722 Cole, J. W. and K. D. Spinks (2009), Caldera volcanism and rift structure in the Taupo
723 Volcanic Zone, New Zealand, *Geological Society, London, Special Publications*, 327,
724 9–29, doi:10.1144/SP327.2.

725 Cox, S. F. and M. A. Etheridge (1983), Crack-seal fibre growth mechanisms and their
726 significance in the development of oriented layer silicate microstructures,
727 *Tectonophysics* , 92, 147-170, doi:10.1016/0040-1951(83)90088-4.

728 Davatzes, N. C. and S. H. Hickman (2010), Stress, fracture, and fluid-flow analysis using
729 acoustic and electrical image logs in hot fractured granites of the Coso Geothermal
730 Field, California, U.S.A., in Dipmeter and borehole image log technology, edited by
731 M. Pöppelreiter, C. García-Carballido and M. Kraaijveld, *AAPG Memoir*, 92, 259-
732 293, doi:10.1306/13181288M923134.

733 Davatzes, N. C. and S. H. Hickman (2009), Fractures, stress and fluid flow prior to
734 stimulation of well 27-15, Desert Peak, Nevada, EGS Project, *Proceedings*, 34th
735 *Workshop on Geothermal Reservoir Engineering*.

736 De Bresser, J. H. P. and C. J. Spiers (1997), Strength characteristics of the *r*, *f*, and *c* slip
737 systems in calcite, *Tectonophysics*, 272, 1-23, doi:10.1016/S0040-1951(96)00273-9.

738 Dempsey, D., J. Rowland, R. Archer (2012), Modelling geothermal fluid flow and silica
739 deposition along an active fault, *Proceedings*, 37th *Workshop on Geothermal*
740 *Reservoir Engineering*.

741 Dezayes, C., A. Genter and B. T. Valley (2010), Structure of the low permeable naturally
742 fractured geothermal reservoir at Soultz, *Comptes Rendus Geoscience*, 342, 517–530,
743 doi:10.1016/j.crte.2009.10.002.

744 Dobson, P. F., T. J. Kneafsey, J. Hulen and A. Simmons (2003), Porosity, permeability, and
745 fluid flow in the Yellowstone geothermal system, Wyoming, *Journal of Volcanology
746 and Geothermal Research*, 123, 313-324.

747 Dromgoole, E. L. and L. M. Walter (1990), Iron and manganese incorporation into calcite:
748 Effects of growth kinetics, temperature and solution chemistry, *Chemical Geology*,
749 81, 311-336.

750 Durney, D. W. and J. G. Ramsay (1973), Incremental strains measured by syntectonic crystal
751 growths, in *Gravity and Tectonics*, edited by K. A. De Jong and R. Scholten, 67-96.

752 Ferrill, D. A. (1991), Calcite twin widths and intensities as metamorphic indicators in natural
753 low-temperature deformation of limestone, *Journal of Structural Geology*, 13, 667-
754 675, doi: 10.1016/0191-8141(91)90029-I.

755 Ferrill, D. A., A. P. Morris, M. A. Evans, M. Burkhard, R. H. Groshong Jr. and C. M. Onasch
756 (2004), Calcite twin morphology: a low-temperature deformation geothermometer,
757 *Journal of Structural Geology*, 26, 1521-1529, doi:10.1016/j.jsg.2003.11.028.

758 Folk, R. L. (1974), The natural history of crystalline calcium carbonate: Effect of magnesium
759 content and salinity, *Journal of Sedimentary Petrology*, 44, 40-53.

760 Fournier, R. O. (1985), Carbonate transport and deposition in the epithermal environment,
761 *Reviews in Economic Geology*, 2, 63-71.

762 Friedman, M. and N. G. Higgs (1981), Calcite Fabrics in Experimental Shear Zones, in
763 *Mechanical Behaviour of Crustal Rocks: The Handin Volume*, edited by N.L. Carter,
764 M. Friedman, J.M. Logan and D.W. Stearns, American Geophysical Union,
765 Washington, D. C., doi:10.1029/GM024p0011.

766 Genter, A., H. Traineau (1996), Analysis of macroscopic fractures in granite in the HDR
767 geothermal well EPS-1, Soultz-sous-Forêts, France, *Journal of Volcanology and*
768 *Geothermal Research*, 72, 121-141.

769 Genter, A., K. Evans, N. Cuenot, D. Fritsch, B. Sanjuan (2010), Contribution of the
770 exploration of deep crystalline fractured reservoir of Soultz to the knowledge of
771 enhanced geothermal systems (EGS), *Comptes Rendus Geoscience*, 342, 502-516.

772 González-Casado, J. M. and C. García-Cuevas (1999), Calcite twins from microveins as
773 indicators of deformation history, *Journal of Structural Geology*, 21, 875-889,
774 doi:10.1016/S0191-8141(99)00081-4.

775 Groshong, R. H. (1972), Strain calculated from twinning in calcite, *Geological Society of*
776 *America Bulletin*, 83, 2025-2038, doi:10.1130/0016-
777 7606(1972)83[2025:SCFTIC]2.0.CO;2.

778 Groshong, R. H., L. W. Teufel and C. Gasteiger (1984), Precision and accuracy of the calcite
779 strain-gage technique, *Geological Society of America Bulletin*, 95, 357-363,
780 doi:10.1130/0016-7606(1984)95<357:PAAOTC>2.0.CO;2.

781 Halfpenny, A. (2010), Some important practical issues for the collection and manipulation of
782 electron backscatter diffraction (EBSD) data from geological samples, *Journal of the*
783 *Virtual Explorer*, 35, doi: 10.3809/jvirtex.2011.00272.

784 Hébert, R. L., B. Ledésert, A. Genter, D. Bartier, C. Dezayes (2011), Mineral precipitation in
785 geothermal reservoir: The study case of calcite in the Soultz-sous-Forêts enhanced
786 geothermal system, *Proceedings, Thirty-Sixth Workshop on Geothermal Reservoir*
787 *Engineering, SGP-TR-191*.

788 Hedenquist, J. W., R. W. Henley (1985), Effect of CO₂ on freezing point depression
789 measurements of fluid inclusions - evidence from active systems and implications for
790 epithermal mineralization, *Economic Geology*, 80, 1379-1406.

- 791 Hedenquist, J. W. (1990), The thermal and geochemical structure of the Broadlands-Ohaaki
792 geothermal system, New Zealand, *Geothermics*, 19, 151-185.
- 793 Hilgers, C., D. Koehn, P. D. Bons and J. L. Urai (2000), Development of crystal morphology
794 during unitaxial growth in a progressively widening vein: II. Numerical simulations of
795 the evolution of antitaxial fibrous veins, *Journal of Structural Geology*, 23, 873-885,
796 doi:10.1016/S0191-8141(00)00160-7.
- 797 Hilgers, C., K. Dilg-Gruschinski and J. L. Urai (2004), Microstructural evolution of syntaxial
798 veins formed by advective flow, *Geology*, 32, 261-264.
- 799 Hurst, A. W., H. M. Bibby and R. R. Robinson (2002), Earthquake focal mechanisms in the
800 central Taupo Volcanic Zone and their relation to faulting and deformation. *New*
801 *Zealand Journal of Geology and Geophysics*, 45, 527-536,
802 doi:10.1080/00288306.2002.9514989.
- 803 Hurst, T., S. Bannister, R. Robinson and B. Scott (2008), Characteristics of three recent
804 earthquake sequences in the Taupo Volcanic Zone, New Zealand. *Tectonophysics*
805 452, 17- 28, doi:10.1016/j.tecto.2008.01.017.
- 806 Krupp, R. E. and T. M. Seward (1987), The Rotokawa geothermal system, New Zealand; an
807 active epithermal gold-depositing environment, *Economic Geology*, 82, 1109-1129,
808 doi:10.2113/gsecongeo.82.5.1109.
- 809 Lacombe, O. and P. Laurent (1992), Determination of principal stress magnitudes using
810 calcite twins and rock mechanics data, *Tectonophysics*, 202, 83-93, doi:10.1016/0040-
811 1951(92)90456-G.
- 812 Lefauchaux, F., M. C. Robert and A. Authier (1973), Étude des défauts créés lors de
813 perturbations extérieures imposées au cours de la croissance hydrothermale de calcite,
814 *Journal of Crystal Growth*, 19, 329-337, doi:10.1016/0022-0248(73)90057-2.

815 Lefauchaux, F. and M. C. Robert (1977), Defects revealing two growth processes for a face
816 case of hydrothermal synthetic calcite, *Journal of Crystal Growth*, 38, 29-37,
817 doi:10.1016/0022-0248(77)90369-4.

818 Leonard, G. S., J. G. Begg and C. J. N. Wilson (2010), Geology of the Rotorua area: scale
819 1:250,000, *Institute of Geological & Nuclear Sciences 1:250,000 geological map 5*,
820 Institute of Geological & Nuclear Sciences Limited, Lower Hutt, New Zealand.

821 Litchfield, N. J., R. Van Dissen, R. Sutherland, P. M. Barnes, S. C. Cox, R. Norris, R. J.
822 Beavan, R. Langridge, P. Villamor, K. Berryman, M. Stirling, A. Nicol, S. Nodder, G.
823 Lamarche, D. J. A. Barrell, J. R. Pettinga, T. Little, N. Pondard, J. J. Mountjoy and K.
824 Clark (2014), A model of active faulting in New Zealand, *New Zealand Journal of*
825 *Geology and Geophysics*, 57, 32-56, doi:10.1080/00288306.2013.854256.

826 Marrett, R. and Laubach, S. E. (1997), Diagenetic controls on fracture permeability and
827 sealing, *International Journal of Rock Mechanics and Mining Sciences*, 34.

828 Massiot, C., McNamara, D. D., Nicol, A., Townend, J., (2015), Fracture width and spacing
829 distributions from borehole televiewer logs and core in the Rotokawa Geothermal
830 Field, New Zealand, *Proceedings World Geothermal Congress 2015*.

831 McLean K. and D. D. McNamara (2011), Fractures interpreted from acoustic formation
832 imaging technology: correlation to permeability, *Proceedings, Thirty-Sixth Workshop*
833 *on Geothermal Reservoir Engineering*, SGP-TR-191.

834 McNamara, D. D., D. Faulkner and E. McCarney (2014), Rock properties of greywacke
835 basement hosting geothermal reservoirs, New Zealand: Preliminary results,
836 *Proceedings, Thirty-Ninth Workshop on Geothermal Reservoir Engineering*, SGP-
837 TR-202.

838 McNamara, D. D., Massiot, C., Lewis, B. and Wallis, I. C. (2015), Heterogeneity of structure
839 and stress in the Rotokawa Geothermal Field, New Zealand, *Journal of Geophysical*
840 *Research*, 120, 1243-1262, doi: 10.1002/2014JB011480.

841 Milicich, S. D., C. J. N. Wilson, G. Bignall, B. Pezaro, C. Bardsley (2013), Reconstructing
842 the geological and structural history of an active geothermal field: A case study from
843 New Zealand, *Journal of Volcanology and Geothermal Research*, 262, 7-24,
844 doi:10.1016/j.jvolgeores.2013.06.004.

845 Milicich, S. D., C. Bardsley, G. Bignall, C. J. N. Wilson (2014), 3-D interpretive modelling
846 applied to the geology of the Kawerau geothermal system, Taupo Volcanic Zone,
847 New Zealand, *Geothermics*, 51, 344-350.

848 Nairn, I. A., S. Beanland (1989), Geological setting of the 1987 Edgecumbe earthquake, New
849 Zealand, *New Zealand Journal of Geology and Geophysics*, 32, 1-13.

850 Nairn, I. A. (2002), Geology of the Okataina Volcanic Centre: scale 1:50,000, *Institute of*
851 *Geological & Nuclear Sciences geological map 25*, Institute of Geological & Nuclear
852 Sciences Limited, Lower Hutt, New Zealand.

853 Nicol, A., J. Walsh, K. Berryman and P. Villamor (2006), Interdependence of fault
854 displacement rates and paleoearthquakes in an active rift, *Geology*, 34, 865
855 doi:10.1130/G22335.1.

856 Nord, G.L. (1994) Transformation-induced twin boundaries in minerals, *Phase Transitions*,
857 48, 107-134.

858 Nüchter J. –A. and B. Stöckhert (2007), Vein quartz microfabrics indicating progressive
859 evolution of fractures into cavities during postseismic creep in the middle crust,
860 *Journal of Structural Geology*, 29, 1445-1462.

861 Okamoto, A. and K. Sekine (2011), Texture of syntaxial quartz veins synthesized by
862 hydrothermal experiments, *Journal of Structural Geology*, 33, 1764-1775.

863 Phillips, W. J. (1972), Hydraulic fracturing and mineralization, *Journal of the Geological*
864 *Society of London*, 128, 337-359.

865 Piazzolo, S., Prior, D.J., Holness, M.D. (2005) The use of combined cathodoluminescence and
866 EBSD analysis: a case study investigating grain boundary migration mechanisms in
867 quartz, *Journal of Microscopy*, 217, 152-161, doi: 10.1111/j.1365-
868 2818.2005.01423.x.

869 Prior, D. J., P. W. Trimby and U. D. Weber (1996), Orientation contrast imaging of
870 microstructures in rocks using forescatter detectors in the scanning electron
871 microscope, *Mineralogical Magazine*, 60, 859-869.

872 Prior D. J., A. P. Boyle, F. Brenker, M. C. Cheadle, A. Day, G. Lopez, L. Peruzzo, G. J.
873 Potts, S. Reddy, R. Spiess, and N. E. Timms (1999), The application of electron
874 backscatter diffraction and orientation contrast imaging in the SEM to textural
875 problems in rocks, *American Mineralogist*, 84, 1741-1759.

876 Ramsay, J. G. (1980), The crack-seal mechanism of rock deformation, *Nature*, 284, 135-139,
877 doi:10.1038/284135a0.

878 Richards, L. and S. A. L. Read (2007), New Zealand greywacke characteristics and
879 influences on rock mass behaviour, *11th Congress of the International Society for rock*
880 *Mechanics*.

881 Rowe, K. J. and E. H. Rutter (1990), Palaeostress estimation using calcite twinning:
882 experimental calibration and application to nature, *Journal of Structural Geology*, 12,
883 1-17.

884 Rowland, J. V. and S. F. Simmons (2012), Hydrologic, magmatic, and tectonic controls on
885 hydrothermal flow, Taupo Volcanic Zone, New Zealand: Implications for the
886 formation of epithermal vein deposits, *Economic Geology*, 107, 427-457,
887 doi:10.2113/econgeo.107.3.427.

888 Sausse, J., M. Fourar and A. Genter (2006), Permeability and alteration within the Soultz
889 granite inferred from geophysical and flow log analysis, *Geothermics*, 35, 544–560,
890 doi:10.1016/j.geothermics.2006.07.003.

891 Seebeck, H., A. Nicol, P. Villamor, J. Ristau and J. Pettinga (2014), Structure and kinematics
892 of the Taupo Rift, New Zealand, *Tectonics*, 33, doi:10.1002/2014TC003569.

893 Sheridan, J., Kovac, K., Rose, P. E., Barton, C., McCulloch, J., Berard, B., Moore, J. M.,
894 Petty, S., Spielman, P., (2003), In situ stress, fracture and fluid flow analysis – East
895 flank of the Coso Geothermal Field, *Proceedings, Twenty-Eighth Workshop on*
896 *Geothermal Reservoir Engineering*, SGP-TR-173.

897 Simmons, S. F. and B. W. Christenson (1994), Origins of calcite in a boiling geothermal
898 system, *American Journal of Science*, 294, 361-400.

899 Steiner, A. (1955), Wairakite, the calcium analogue of analcime, a new zeolite mineral,
900 *Mineralogical Magazine*, 30, 691-698.

901 ten Have, T. and W. Heijnen (1985), Cathodoluminescence activation and zonation in
902 carbonate rocks: an experimental approach, *Geologie en Mijnbouw*, 64, 297–310.

903 Teng, H. H., P. M. Dove and J. J. De Yoreo (2000), Kinetics of calcite growth: Surface
904 processes and relationships to macroscopic rate laws, *Geochimica et Cosmochimica*
905 *Acta*, 64, 2255-226, doi:10.1016/S0016-7037(00)00341-0.

906 Timms, N. E., J. Li and S. M. Reddy (2009), Quantitative microstructural characterization of
907 natrojarosite scale formed during high-pressure acid leaching of lateritic nickel ore.
908 *American Mineralogist*, 94, 1111-1119, doi:10.2138/am.2009.3104 .

909 Townend, J., S. Sherburn, R. Arnold, C. Boese, C. and L. Woods (2012), Three-dimensional
910 variations in present-day tectonic stress along the Australia–Pacific plate boundary in
911 New Zealand, *Earth and Planetary Science Letters*, 353-354, 47–59,
912 doi:10.1016/j.epsl.2012.08.003.

913 Tulloch, A. J. (1982), Mineralogical observations on carbonate scaling in geothermal wells at
914 Kawerau and Broadlands, *Proceedings 4th New Zealand Geothermal Workshop*.

915 Urai, J. L., P. F. Williams and H. L. M. van Roermund (1991), Kinematics of crystal growth
916 in syntectonic fibrous veins, *Journal of Structural Geology*, *13*, 823-836,
917 doi:10.1016/0191-8141(91)90007-6.

918 Villamor, P. and K. R. Berryman (2001), A late Quaternary extension rate in the Taupo
919 Volcanic Zone, New Zealand, derived from fault slip data, *New Zealand Journal of
920 Geology and Geophysics*, *44*, 243-269, doi:10.1080/00288306.2001.9514937.

921 Villamor, P., K. R. Berryman, I. A. Nairn, K. Wilson, N. Litchfield and W. Ries (2011),
922 Associations between volcanic eruptions from Okataina volcanic centre and surface
923 rupture of nearby active faults, Taupo rift, New Zealand: insights into the nature of
924 volcano-tectonic interactions, *Geological Society of America Bulletin*, *123*, 1383-
925 1405.

926 Wallace, L. M., J. Beavan, R. McCaffrey and D. Darby (2004), Subduction zone coupling
927 and tectonic block rotations in the North Island, New Zealand, *Journal of Geophysical
928 Research*, *109*, 1978-2012, doi:10.1029/2004JB003241.

929 Wallis, I. C., D. D. McNamara, J. Rowland and C. Massiot (2012), The nature of fracture
930 permeability in the basement greywacke at Kawerau Geothermal Field, New Zealand,
931 *Proceedings, Thirty-seventh Workshop on Geothermal Reservoir Engineering*, SGP-
932 TR-194.

933 Wilson, C. J. N., B. F. Houghton, M. O. McWilliams, M. A. Lanphere, S. D. Weaver and R.
934 M. Briggs (1995), Volcanic and structural evolution of the Taupo Volcanic Zone,
935 New Zealand: a review, *Journal of Volcanology and Geothermal Research*, *68*, 1-28,
936 doi:10.1016/0377-0273(95)00006-G.

937 Wiltschko, D. V. and J. W. Morse (2001), Crystallization pressure versus “crack seal” as the
938 mechanism for banded veins, *Geology*, 29, 79-82, DOI: 10.1130/0091-7613(2001)
939 029<0079:CPVCSA>2.0.CO;2.

940 Wogelius, R. A., D. G. Fraser, G. R. Wall and G. W. Grime (1997), Trace element and
941 isotopic zonation in vein calcite from the Mendip Hills, UK, with spatial-process
942 correlation analysis, *Geochimica et Cosmochimica Acta*, 61, 2037-2051.

943 Wood, C. P., R. L. Brathwaite and M. D. Rosenberg (2001), Basement structure, lithology
944 and permeability at Kawerau and Ohaaki geothermal fields, New Zealand,
945 *Geothermics*, 30, 461-481, doi:10.1016/S0375-6505(01)00003-7.

946 Xu, M., L. Kovarik, B. W. Arey, A. R. Felmy, K. M. Rosso and S. Kerisit (2014), Kinetics
947 and mechanisms of cadmium carbonate heteroepitaxial growth at the calcite (10-14)
948 surface, *Geochimica et Cosmochimica Acta*, 134, 221-233,
949 doi:10.1016/j.gca.2013.11.036.

950

951

952 **Figure 1** Schematic models of various fracture sealing processes; a) syntaxial sealing,
953 b) antitaxial sealing, c) stretching vein showing both delocalised vein growth
954 (via fracture propagation through wall rock) and localised vein growth
955 (fracture propagation across already deposited material), and d) vein formation
956 from a pressure shadows/fringe occurring next to a rigid object.

957

958 **Figure 2** Map of the Taupo Volcanic Zone showing the major structural features and
959 the location of the Kawerau Geothermal Field. Inset provides geographical
960 context within New Zealand.

961

962 **Figure 3** a) Photograph of drill-core sample of greywacke reservoir rock from the
963 Kawerau Geothermal Field used for study, b) Plane polarised, light
964 microscopy image of the drill core sample. Red boxes outline individual areas
965 selected for focused examination using CL, EDX, and EBSD, c) Cross
966 polarised light microscopy image of the calcite vein from Area 1, d) Cross
967 polarised light microscopy image of the calcite/wairakite vein from Area 2.

968

969 **Figure 4** Cathodoluminescence (CL) images of fractured greywacke reservoir rock
970 from Kawerau Geothermal Field. a) CL image showing cross-cutting calcite
971 and wairakite filled veins. Inset white boxes define areas of zoom in Figure 4b
972 and 4c, b) CL image of a bladed calcite filled vein from the youngest fracture
973 generation. Inset dashed white box represents area of zoom in Figure 4e, c) CL
974 image of a calcite/wairakite filled vein cross-cut by a younger calcite filled
975 vein (white lines mark older generation fracture edges), inset white dashed box
976 represents area of zoom in Figure 4d.

977

978 **Figure 5** a) Fe and Mn EDX count maps of bladed calcite crystals in the younger
979 generation fracture (zone 1 in Figure 3). White lines define the edge of the
980 fracture. b) Ca and Al EDX count maps of a calcite and wairakite sealed older
981 generation fracture (Zone 2 in Figure 3). The dashed white line defines where
982 the older generation fracture is cross-cut by the younger generation fracture.

983

984 **Figure 6** EDX data from a linescan (dashed white line shown in figure 4b) across
985 chemically zoned, bladed calcite crystals sealing the younger fracture
986 generation. Fe, Ca, and Mn element wt% linescan data are plotted as Fe/Ca,

987 Mn/Ca, and Fe+Mn/Ca ratios, such that when ratio = 0, calcite is pure CaCO₃
988 (with respect to Fe and Mn), and when the ratio > 0 there is higher Fe and Mn
989 content in the calcite. a) Graph showing variation in Mn/Ca and Fe/Ca ratios,
990 b) Graph showing variation in Fe+Mn/Ca ratio, c) CL microscopy image of
991 calcite crystals in the younger fracture generation across which linescan data
992 was collected and d) the same area under as a back scattered electron image.

993

994 **Figure 7** EBSD data on calcite fracture fill from the youngest generation of fracturing.
995 a) Band Contrast map with Grain Boundary overlay, b) Band Contrast map
996 with an Inverse Pole Figure colour scale in the sample's Z direction and Grain
997 Boundary overlay, c) Misorientation profiles of Grains 1 and 2 (labelled in 7b)
998 following direction indicated by red arrows, insets are Band Contrast maps
999 with Texture Component overlays for the crystals being profiled (crystal
1000 colour indicates amount of misorientation from a given orientation on the
1001 crystal (blue = 0°, red = 10°), d) Contoured inverse pole figures for
1002 neighbouring calcite misorientations of 2°-5°, 5°-10°, and 75°-80°.

1003

1004 **Figure 8** Contoured pole figures of calcite crystal orientations in the younger generation
1005 fracture using one orientation measurement per calcite crystal (point per grain)
1006 for 1168 crystals. Pole figures are equal area projection, upper hemispheres
1007 and are contoured with a half width of 15° and a cluster size of 5° (Halfpenny,
1008 2010).

1009

1010 **Figure 9** EBSD data on calcite fracture fill from an older generation of fracturing. a)
1011 Band Contrast map with Grain Boundary overlay, b) Band Contrast map with

1012 Inverse Pole Figure (RGB colour scale) and Grain Boundary overlay, c)
1013 Misorientation profile of Grain 1 (labelled in 8b) following direction indicated
1014 by red arrow, inset is Band Contrast map with Texture Component overlays
1015 for the crystal being profiled (colour indicates amount of misorientaion from a
1016 given orientation on the crystal; blue = 0°, red = 10°), d) Contoured inverse
1017 pole figures for neighbouring calcite misorientations of 2°-5°, 5°-10°, and 75°-
1018 80°.

1019

1020 **Figure 10** Misorientation angle distribution analyses. Frequencies of misorientation
1021 angles for neighbour and random pair points for the younger calcite filled
1022 fracture showing a) relative frequency, and b) cumulative frequency.
1023 Frequencies of misorientation angles for neighbour and random pair points for
1024 the older calcite filled fracture showing c) relative frequency, and d)
1025 cumulative frequency.

1026

1027 **Figure 11** a) CL images of two elongate, bladed calcite crystals from the younger
1028 fracture generation, b) EBSD texture component maps of the same two calcite
1029 crystals, c) schematic of the same crystals showing their fast growth direction
1030 (green arrows) and slower growth directions (red arrows). Red dots mark point
1031 where texture component map misorientations are scaled from, black lines =
1032 >10° misorientation boundaries (grain boundaries), purple lines = calcite twin
1033 boundaries, and yellow lines = sub-grain boundaries (2 - 5° misorientation).

1034

1035 **Figure 12** Graph showing the determined relationship between differential stress and the
1036 log number of twins/mm in calcite crystals (from Rowe and Rutter, 1990) with

1037 two of the twin sets densities observed from calcite crystals in the older
1038 generation, wairakite/calcite sealed fracture.

1039

1040 **Figure 13** Plane polarised light microscopy picture of the younger generation fracture
1041 sealed with bladed calcite. Inset is a contoured pole figure of the orientations
1042 of calcite crystal's c-axes (using one orientation point per crystal) within the
1043 dashed box (Area 1). Red arrows show the preferred orientation of the c-axes
1044 on the pole figure and the direction of extension on the photograph
1045 (determined from the c-axes preferred orientation).

Figure
[Click here to download high resolution image](#)

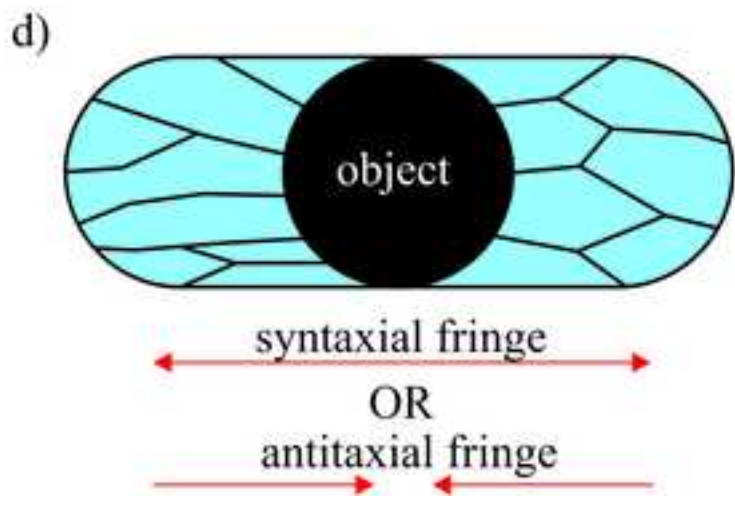
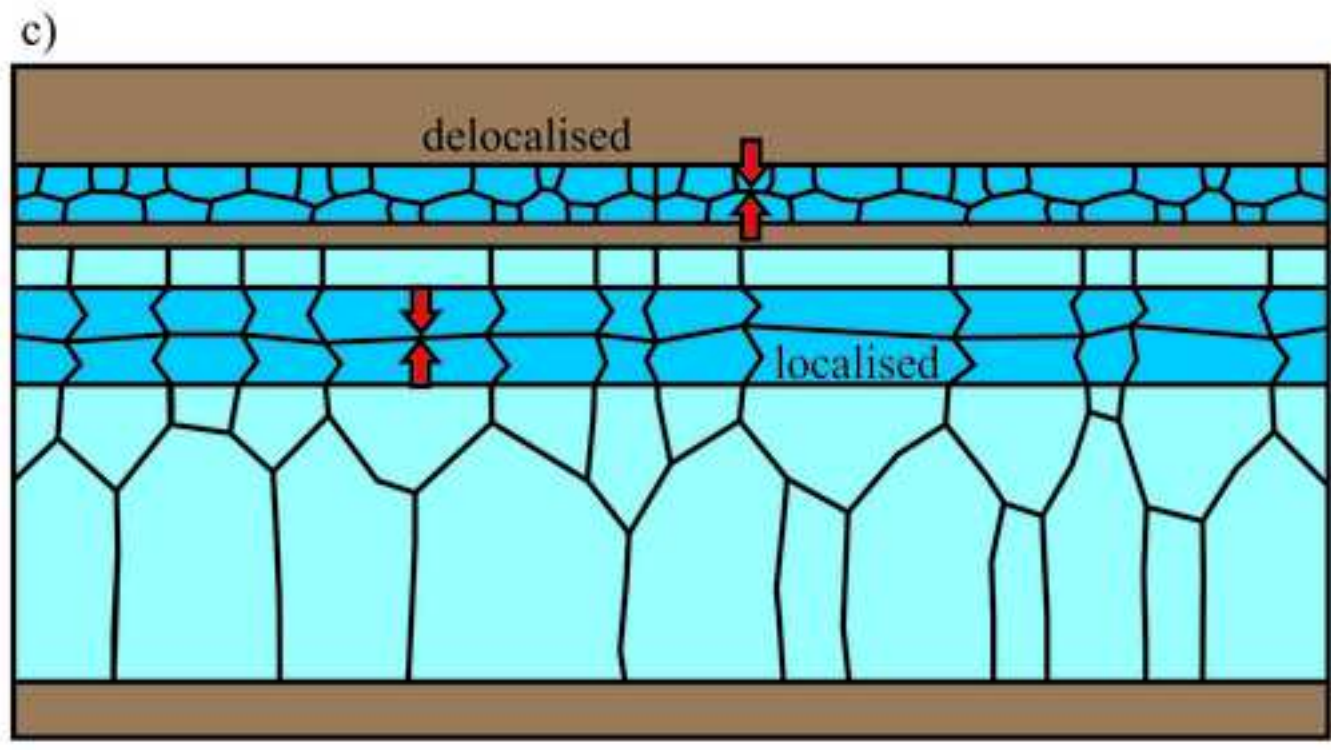
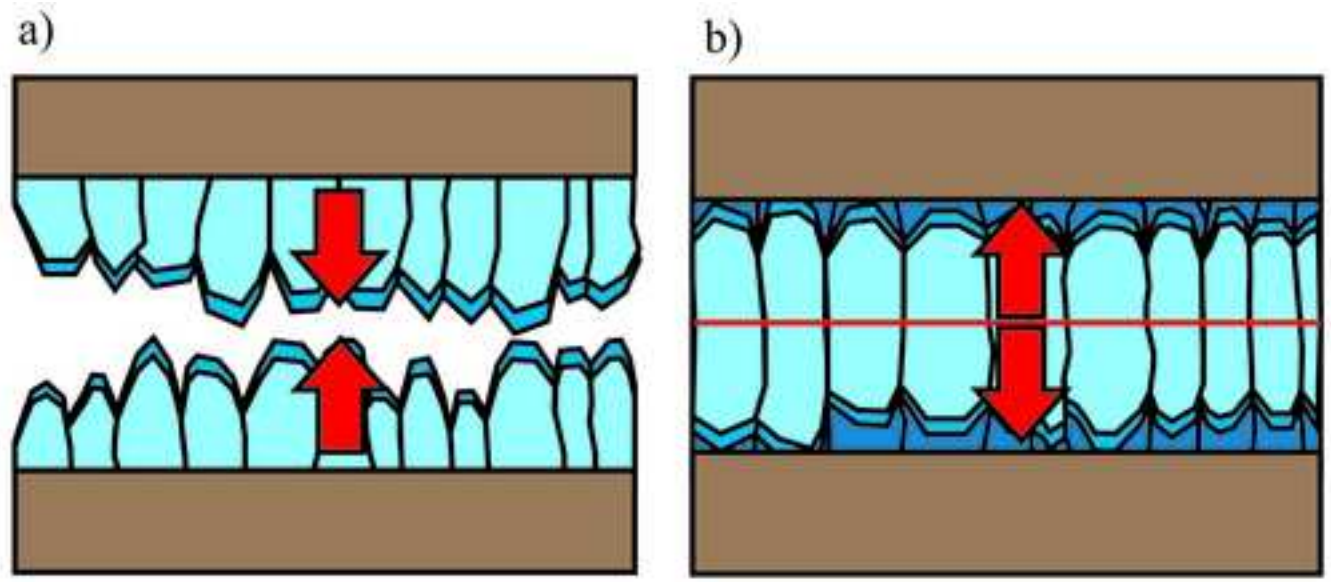


Figure
[Click here to download high resolution image](#)

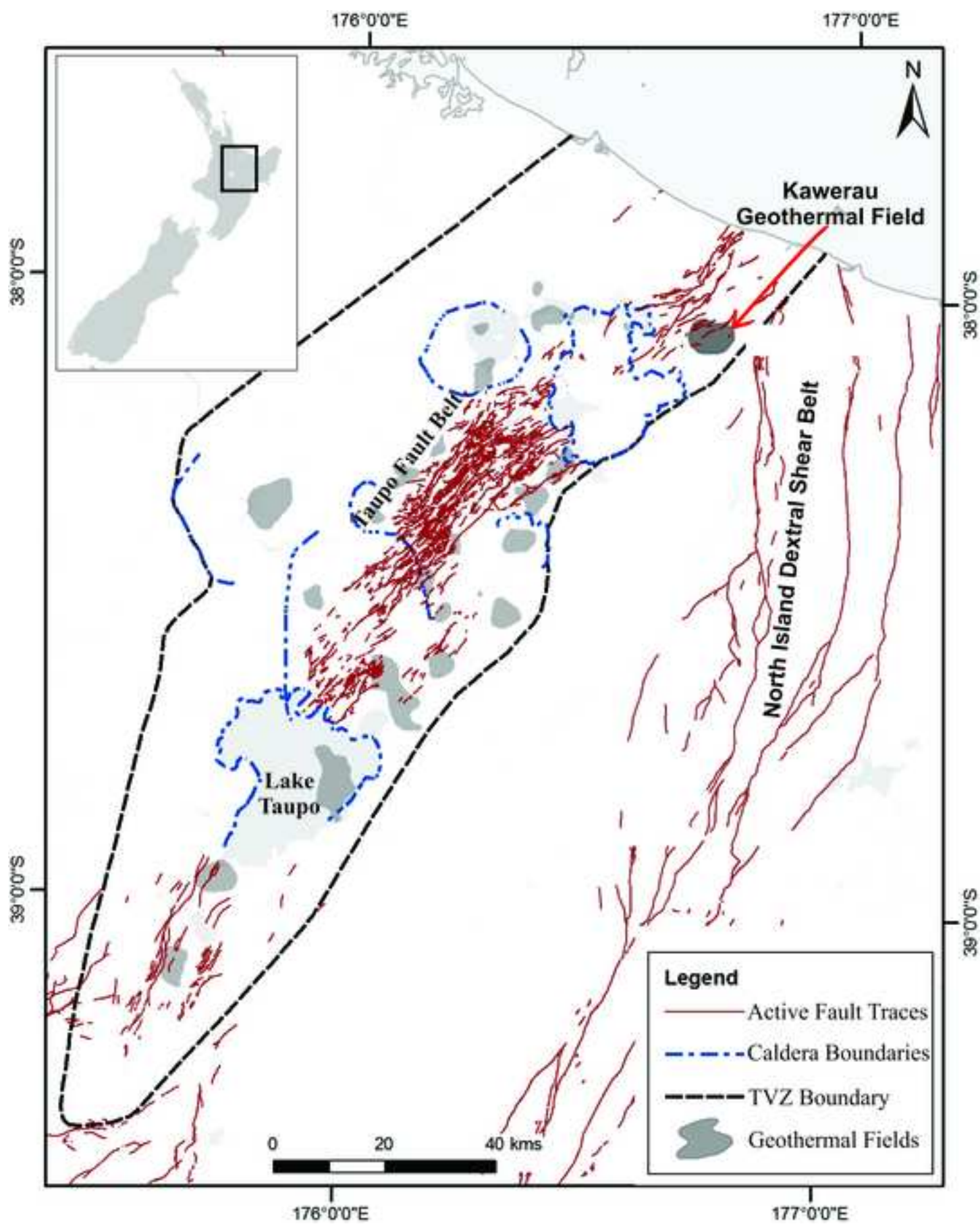


Figure
[Click here to download high resolution image](#)

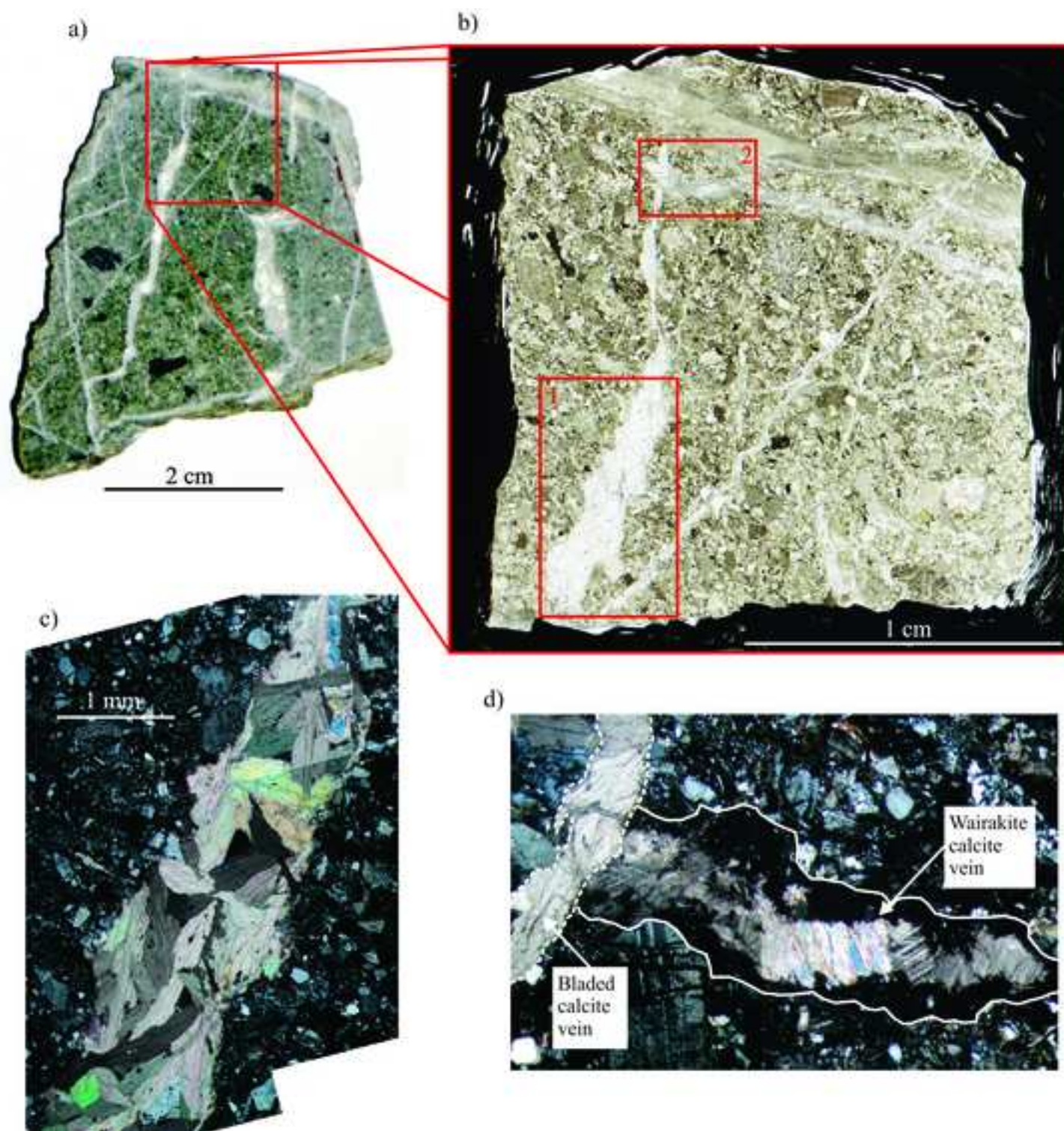


Figure
[Click here to download high resolution image](#)

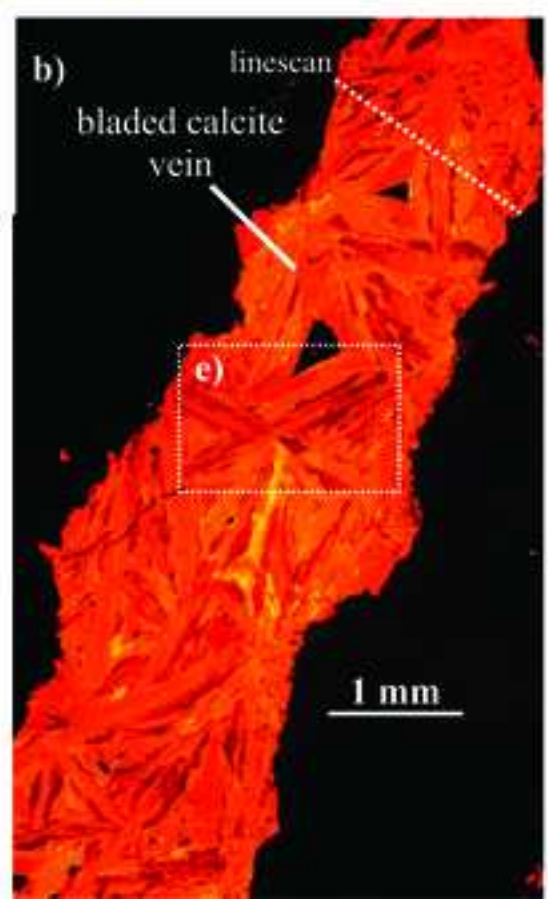
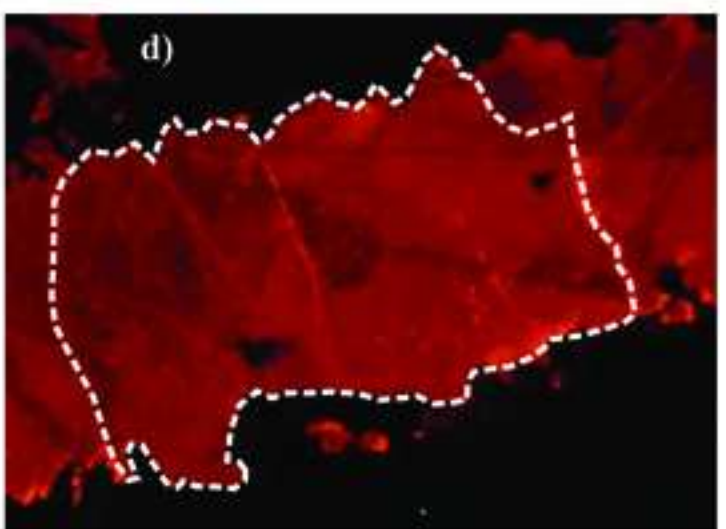
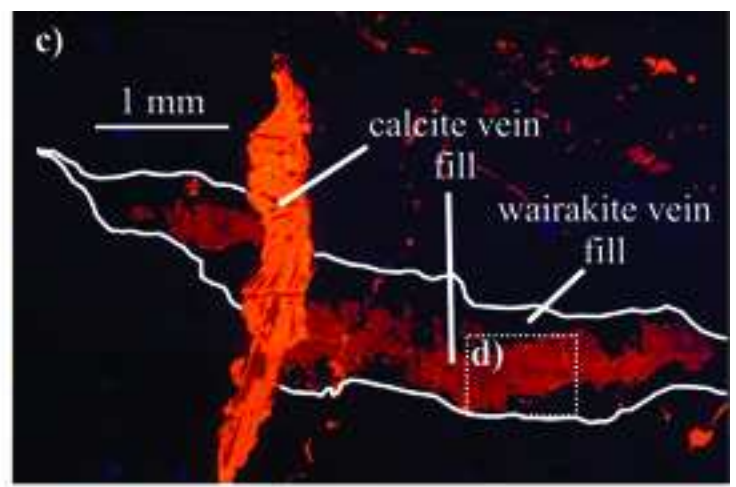
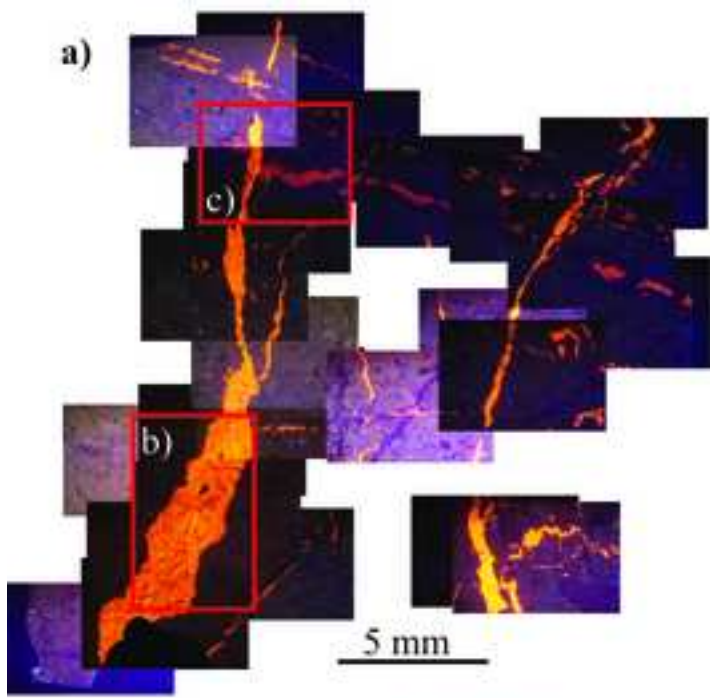


Figure
[Click here to download high resolution image](#)

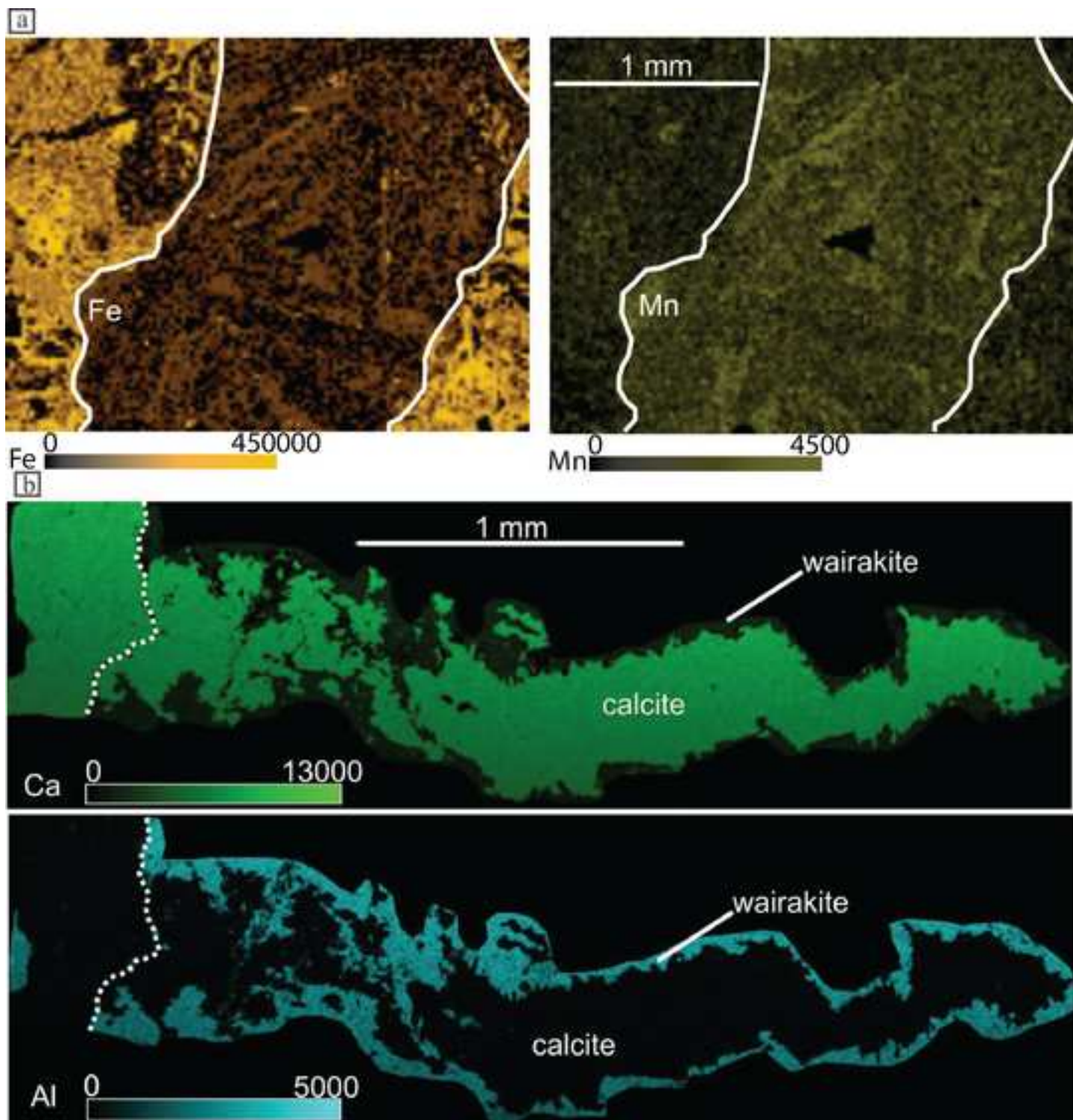


Figure
[Click here to download high resolution image](#)

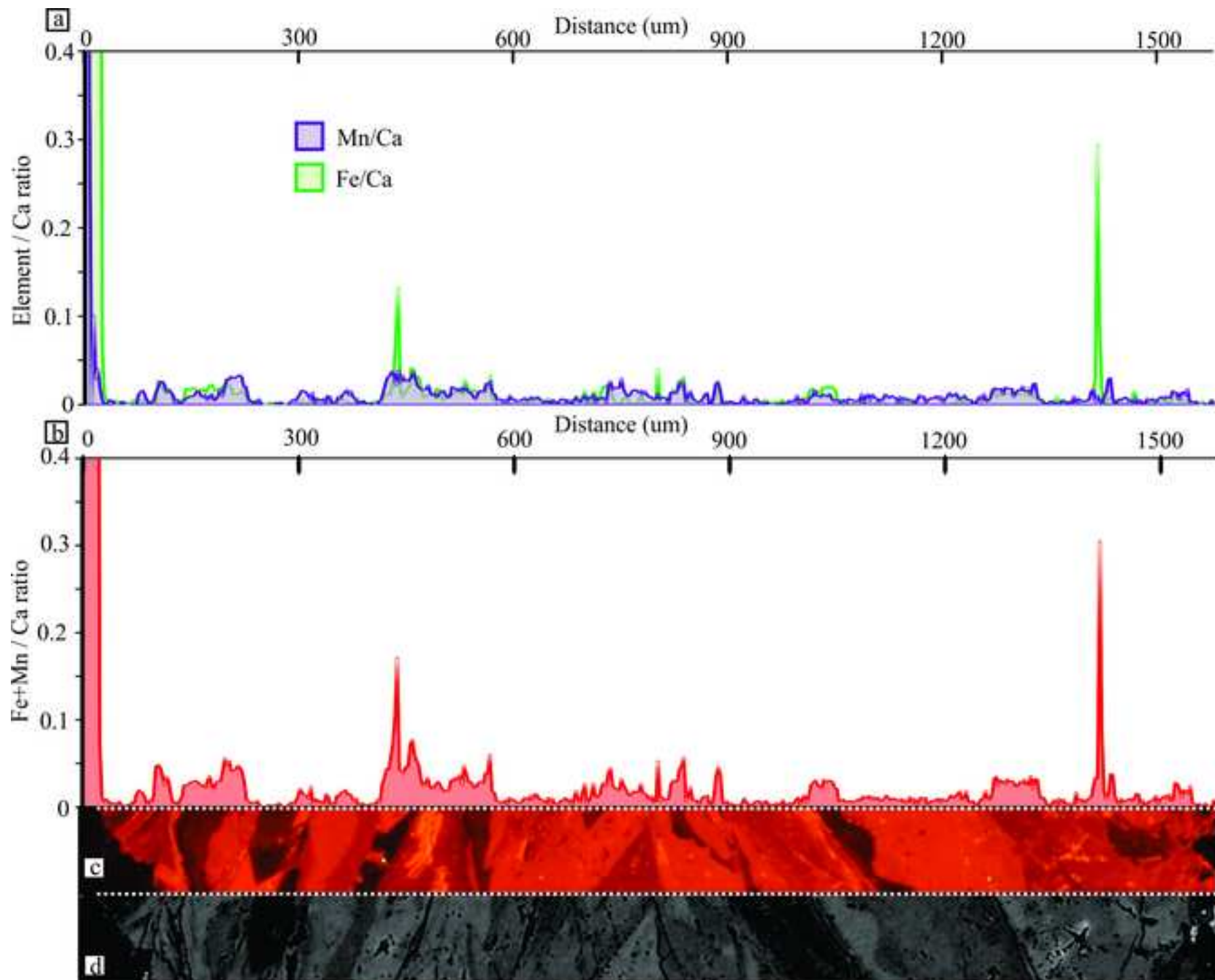
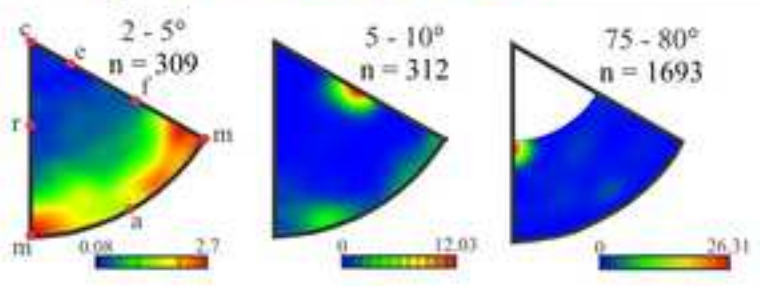
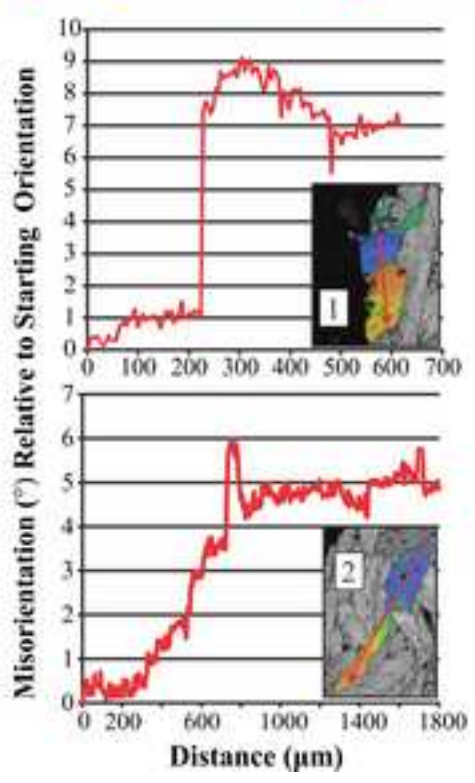
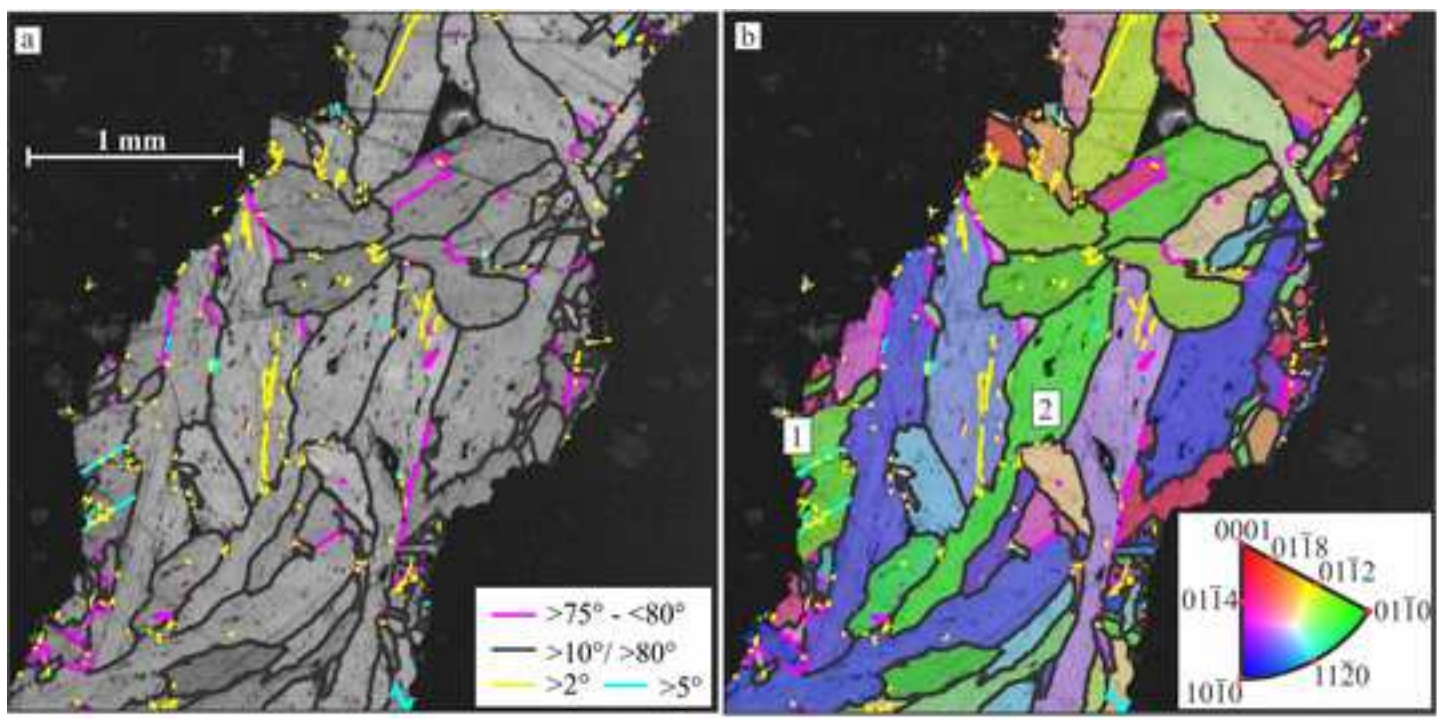


Figure
[Click here to download high resolution image](#)



Figure

[Click here to download high resolution image](#)

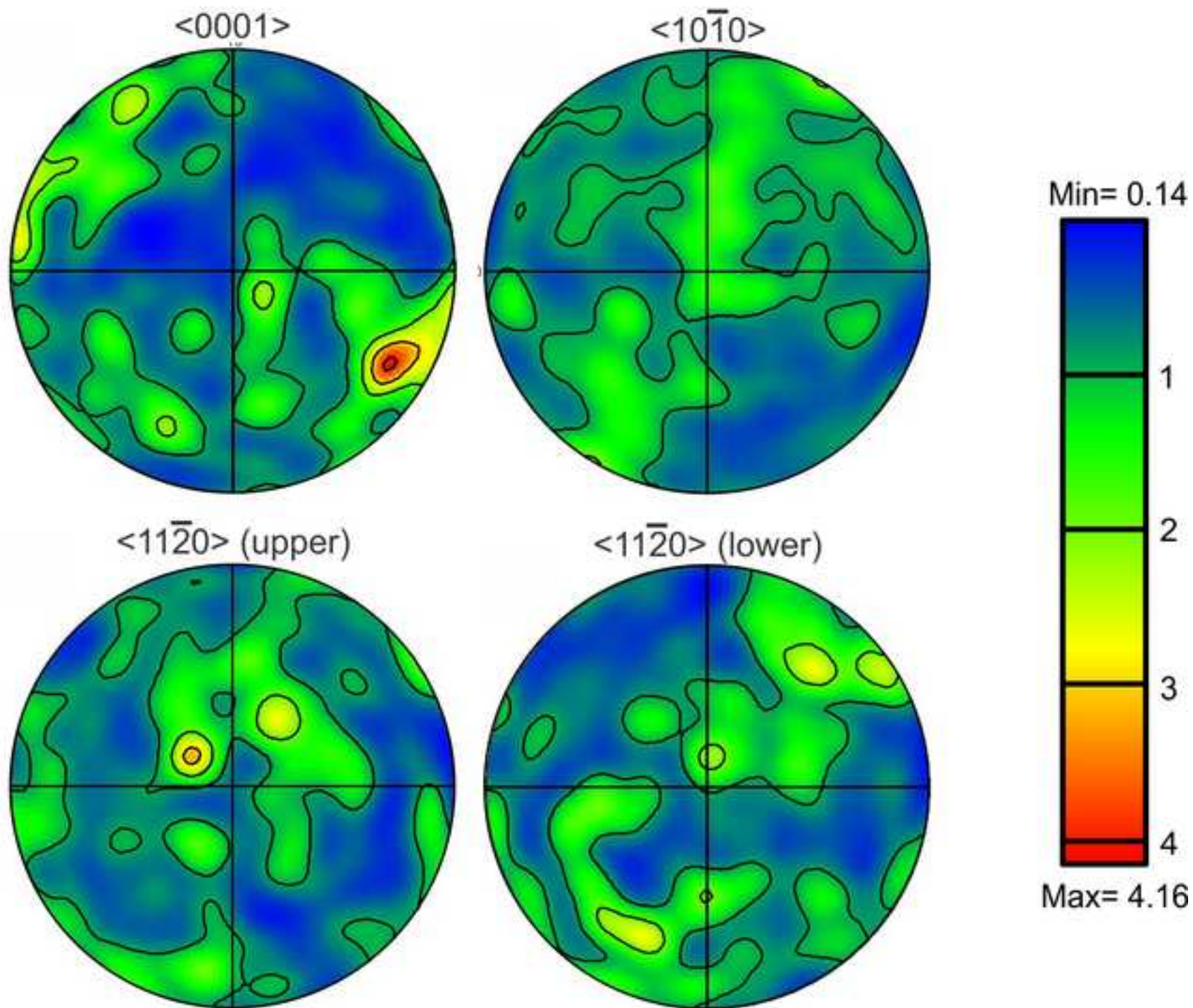


Figure
[Click here to download high resolution image](#)

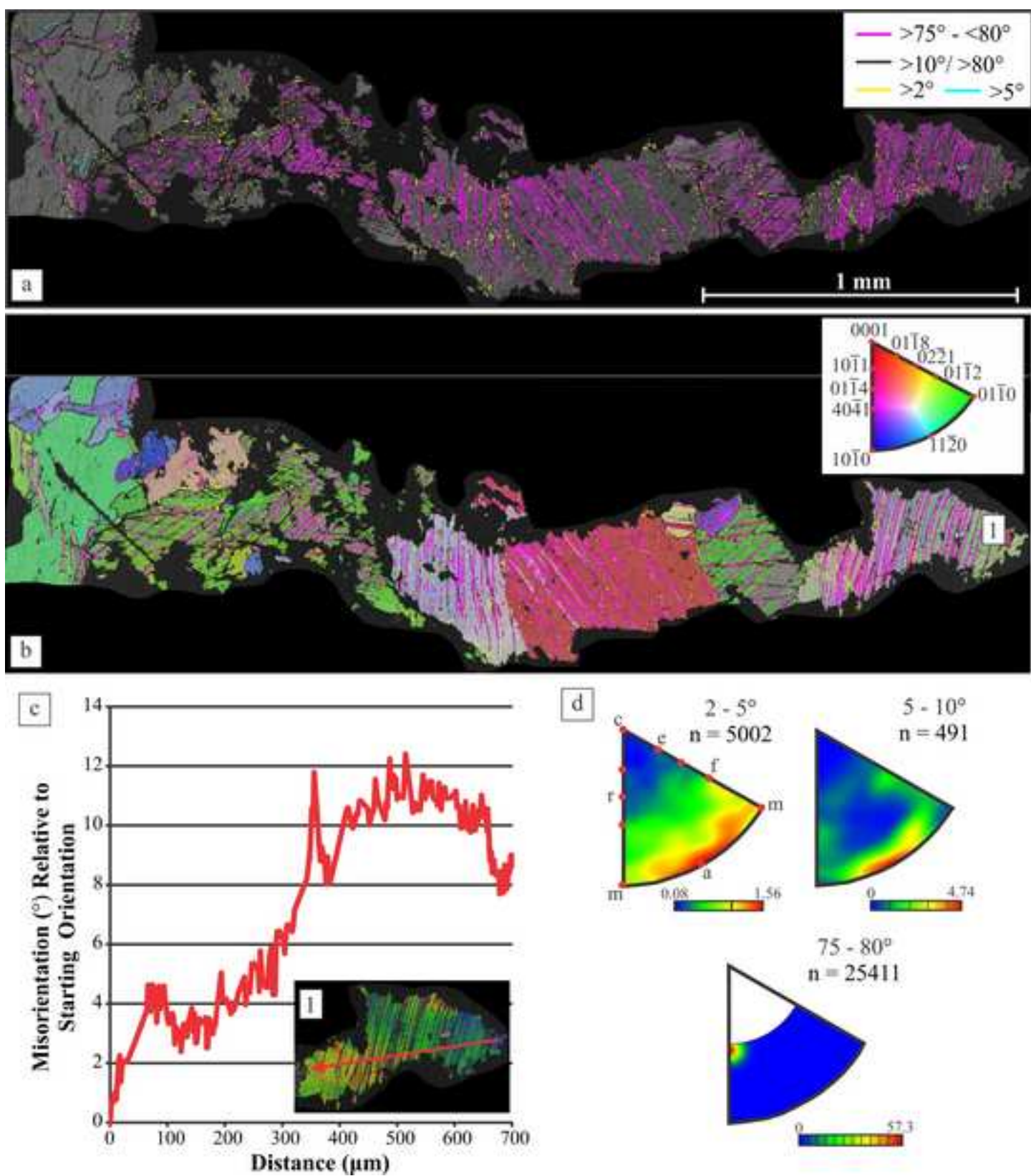
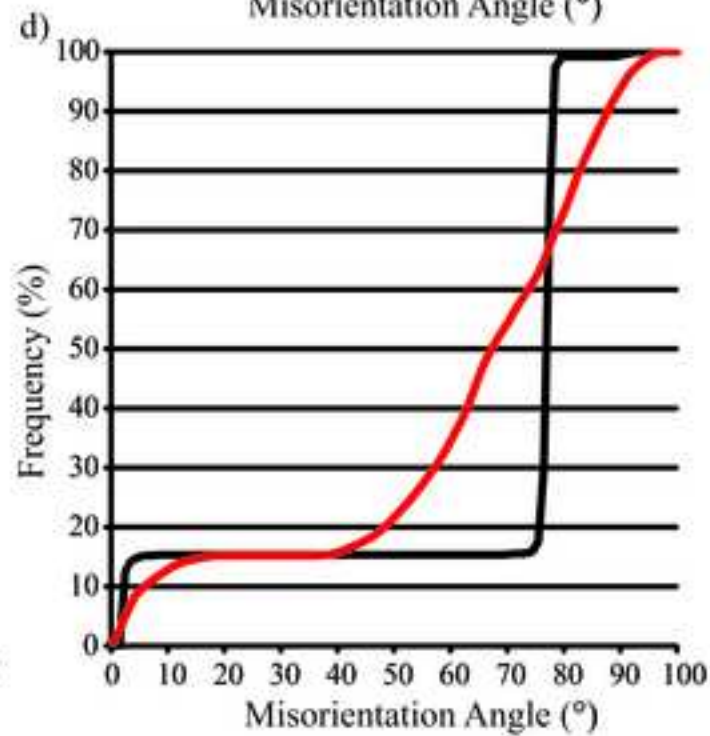
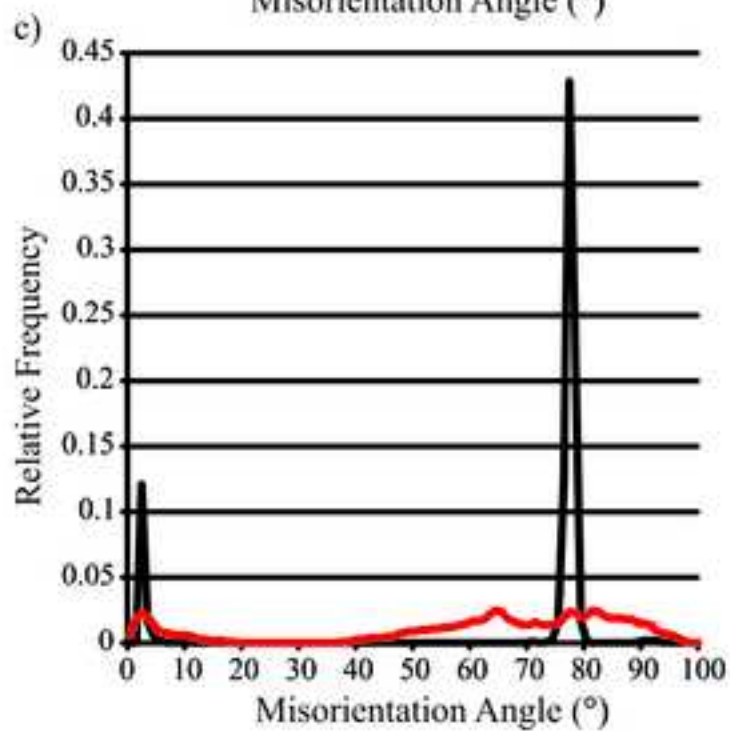
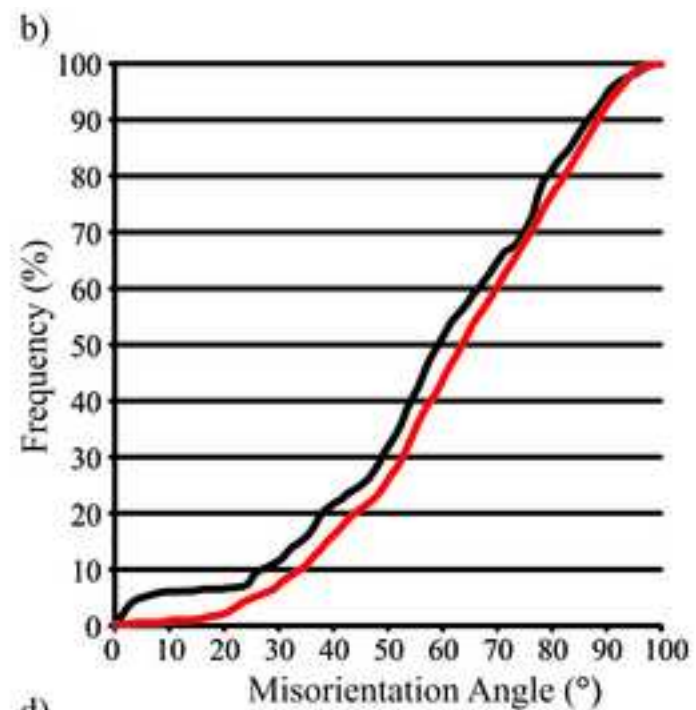
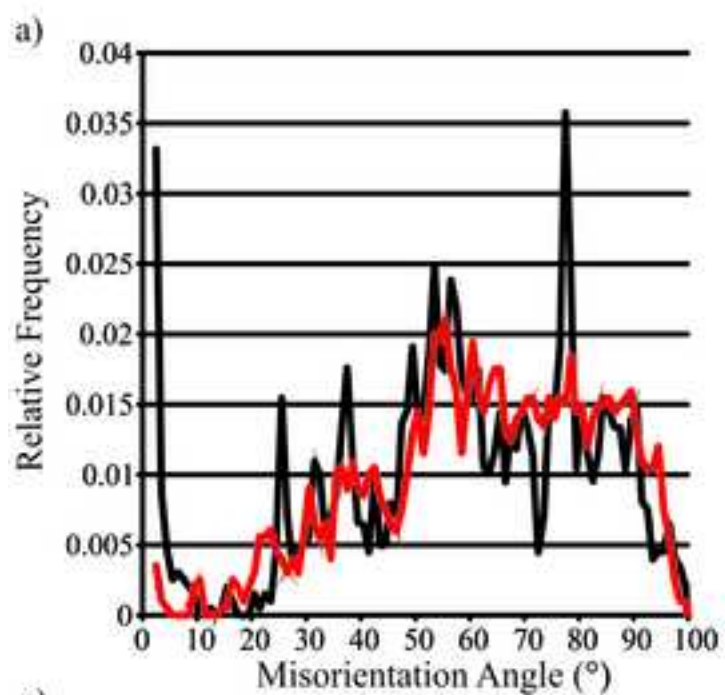


Figure
[Click here to download high resolution image](#)



— Neighbour Pair — Random Pair

Figure
[Click here to download high resolution image](#)

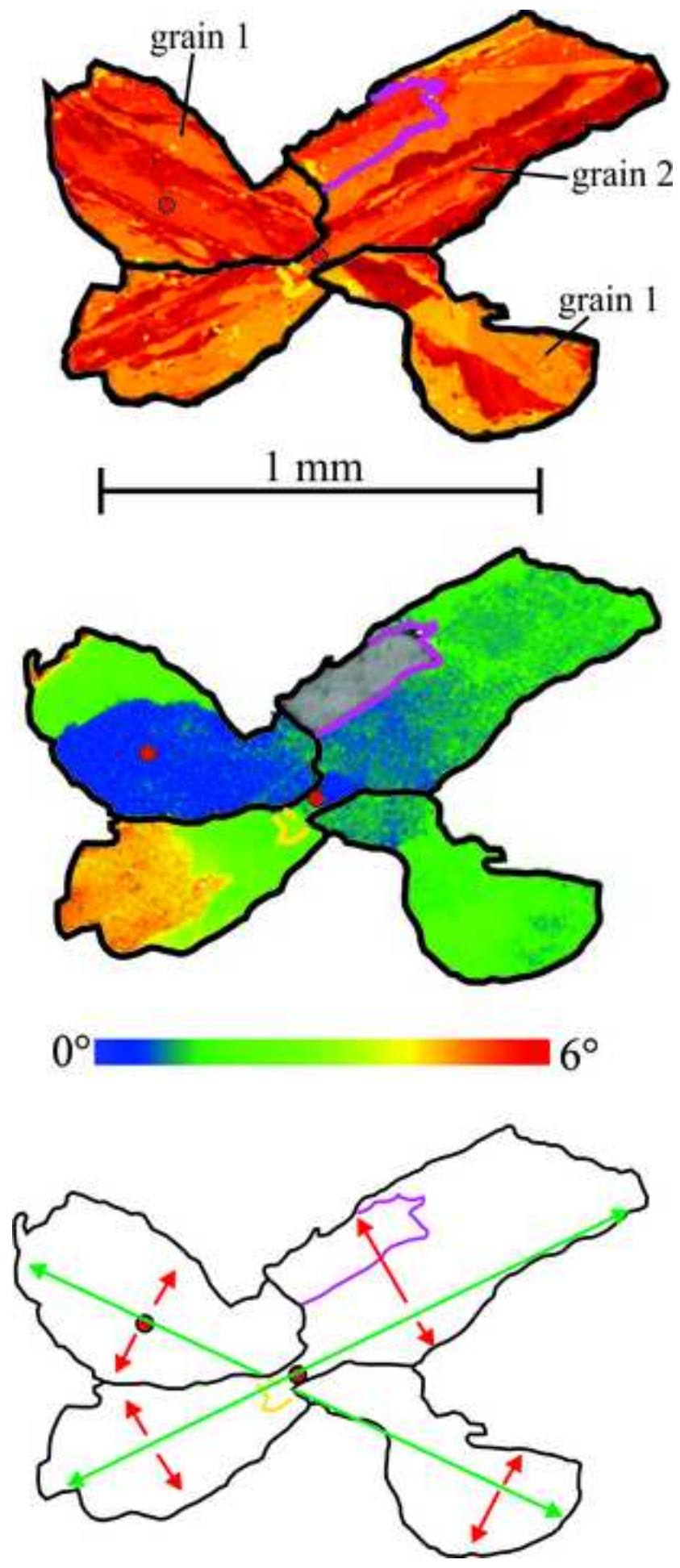
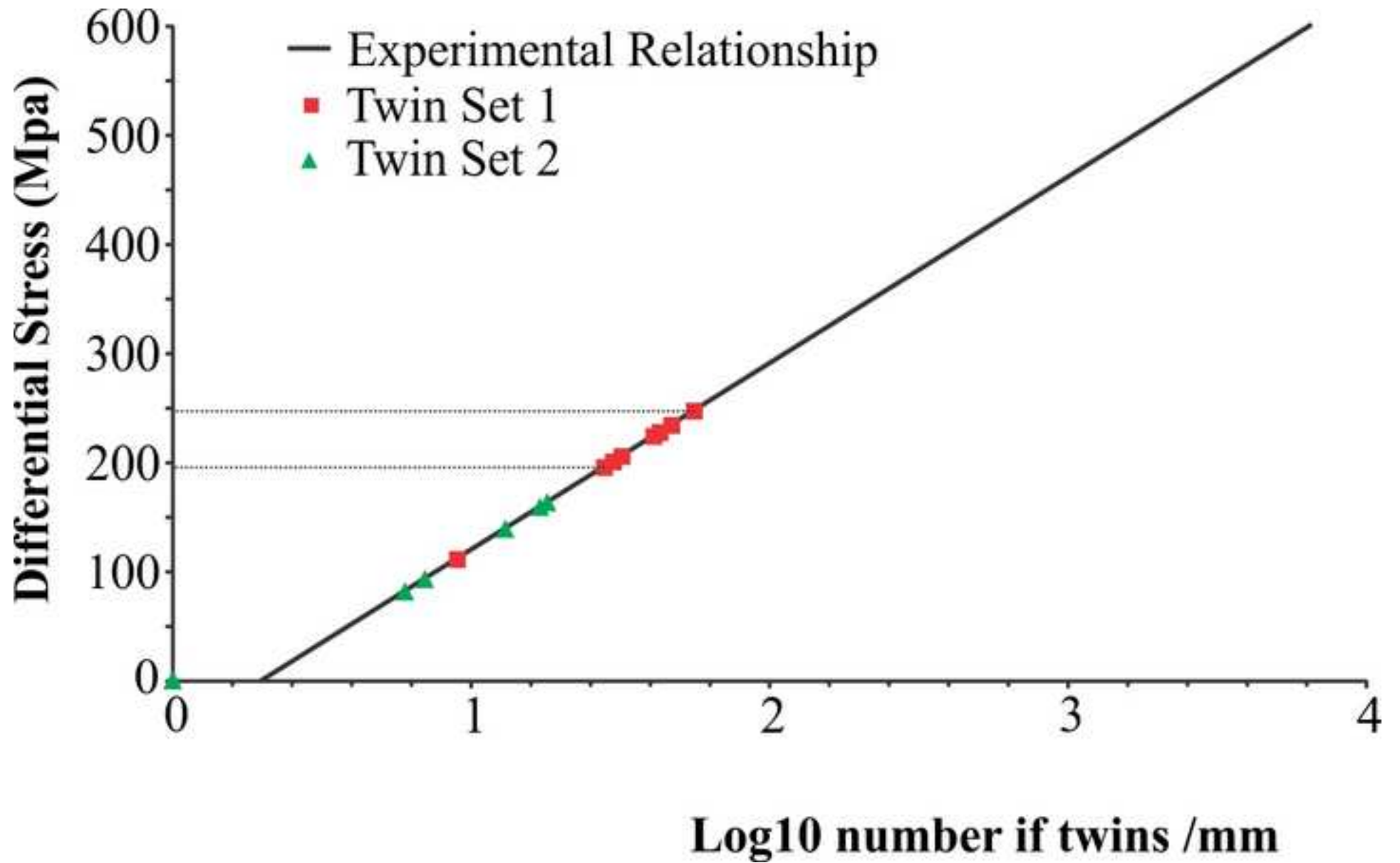


Figure
[Click here to download high resolution image](#)



Figure

[Click here to download high resolution image](#)

